


Vortical cleaning of oil-impregnated porous surfaces

Siddhant Jain , Shubham Sharma, Durbar Roy, and Saptarshi Basu*

Department of Mechanical Engineering, Indian Institute of Science, Bangalore 560012, India



(Received 26 October 2022; accepted 8 March 2023; published 14 April 2023)

We investigate the cleaning mechanism of an oil-impregnated porous surface by utilizing a method of vortex ring interaction. The kinetic energy of a vortex ring is exploited to expunge the trapped oil from the spherical-bead-based porous surface. Qualitative and quantitative measurements were made using high-speed shadowgraphy imaging, planar laser-induced fluorescence (PLIF) imaging, and particle image velocimetry (PIV) techniques. The interaction phenomenon is explored from the perspective of vortex ring dynamics followed by oil sheet dynamics. Five different strengths of a vortex ring [characterized by the circulation (Γ)-based Reynolds number ($\text{Re}_\Gamma = 2550\text{--}14\,260$: $\text{Re}_\Gamma = \Gamma/\nu$, where ν is the kinematic viscosity)] and two types of surface porosity (ϕ) (open area ratio, 0.21 and 0.41) are considered for parametric analysis. The interaction process with oil is divided into three regimes: (i) penetration, (ii) bag formation, and (iii) bag breakup. Depending on the strength of the vortex ring, it is observed that surface cleaning takes place from both upstream and downstream regions of the porous surface. The vortex rings with higher Re_Γ can expunge more oil through a complicated interaction process involving Rayleigh-Taylor- and Rayleigh-Plateau-type instabilities. However, along with Re_Γ , the interaction dynamics depend strongly on the shape and ϕ value. The interaction process is characterized by vorticity cancellation, Kelvin-Helmholtz (KH) instabilities, and three-dimensional interactions.

DOI: [10.1103/PhysRevFluids.8.044701](https://doi.org/10.1103/PhysRevFluids.8.044701)

I. INTRODUCTION

Vortex rings are a self-sustainable system of rotating fluid that can propel to longer distances before diffusing into their surrounding. They are ubiquitously present and can be observed as smoke rings, mushroom clouds during explosions [1], jellyfish locomotion [2], microburst phenomena [3], cardiac relaxation of the human heart [4], and more. There are various ways of generating a vortex ring; however, in a laboratory environment, they are generally created using piston-cylinder or solenoid valve arrangement. A plethora of work can be found on the fundamental physics of vortex rings [1,5–13]. The interaction of vortex rings with porous surfaces has been studied by a relatively smaller section of the scientific community. Adhikari and Lim [14] considered uniform screens having a constant wire diameter (0.2 mm) with two ϕ values (62% and 81%) and Re_Γ ranging from 384 to 2369. At the lowest Re value, the ring failed to pass through the screen. However, at the highest tested Re value, the ring passed through the screen as a modified ring propelling at a lower speed. Hryniuk *et al.* [15] considered a single ϕ (64%) and three values of formation Re (2300, 3800, and 4200), and they observed that placing a porous screen downstream did not affect the formation and initial motion of the vortex ring. The vortex ring reformed only in the case of fine mesh, and it became chaotic in the case of larger diameters due to the formation of small-scale vortical substructures. Moreover, the interaction Re value matched the vortex shedding Re value for circular cylinders. Naaktgeboren *et al.* [16] varied ϕ (0.44 to 0.79) and Re (based on jet diameter,

*Corresponding author: sbasu@iisc.ac.in

3000 and 6000), and they observed that nearly all the kinetic energy of the vortex ring was lost during the interaction process. Cheng *et al.* [17] investigated the problem by carrying out numerical simulations on a wide range of parameters, and they reported that both reducing ϕ and increasing the thickness impeded vorticity transmission through the porous surface, whereas increasing Re or ϕ enhanced the vorticity transmission. Musta and Krueger [18] gave an account of the energy decay process due to interactions of vortex rings with multiple screens. Mujal-Colilles *et al.* [19] studied the interaction of vortex rings with a thick permeable foam (25–50 mm) at $Re_T = 2000$, and they showed that the vortex could not transmit downstream in any of the cases. A detailed study on the effect of Re at interaction (defined by the wire diameter and the convection speed of the vortex ring near the interaction site) on the transmitted vortex ring is presented by Hrynuk *et al.* [20], where they argue that the transmitted vortex ring is a function of vortex shedding behavior and not screen porosity. An *et al.* [21] found that ϕ played an important role in disrupting vortical structures, and they emphasized the limitations of using evenly arranged rods. As an active flow control system, Xu *et al.* [22] studied the effect of porous surface geometry on the interaction dynamics by maintaining a constant porosity of 75% and varying the hole diameters. A larger diameter decreased the coherence of the transmitted vortex that was attributed to lesser vorticity cancellation and enhanced Kelvin-Helmholtz (KH) instability. The velocity triple decomposition was employed to show the kinetic energy transfer from a large-scale coherent structure to the small-scale turbulent structures present in the downstream field. In terms of the quality of the downstream flow field, the case with the largest hole diameter resulted in minimum energy fluctuations, making it suitable for flow control applications. A similar study on laminar vortex rings suggests a self-similar characteristic of velocity profiles (similar to that of a synthetic jet) at the far downstream location from the interaction region, irrespective of the geometry of the porous surface [23]. They further showed that with a decrease in hole diameter, there was an increase in the time-mean drag of a porous surface. The effect of Re was studied by Li *et al.* [24] by employing the triple decomposition method. At higher Re values, a loss of coherence in the transmitted vortex was observed due to the transition from the laminar to the turbulent regime, resulting in the large energy fluctuations. Also, KH vortices were observed at higher Re values in the trailing jets that ultimately led to a loss of coherence in the primary vortex ring. Li *et al.* [25] proposed a similarity parameter to characterize the loss of jet momentum flux, kinetic energy, and circulation due to its interaction with a porous surface. Recently, Xu *et al.* [26] studied the influence of porosity on the vortex-surface interaction characteristics of a synthetic vortex. The transmitted flow structures were shown to be strongly influenced by both Re and porosity values. Flow evolution involving the occurrence of finger-type jets, vorticity cancellation, coherency of a transmitted vortex ring, the occurrence of KH instability, and more were discussed. The loss of momentum flux due to interaction was shown to exhibit a linear relationship with the surface porosity, irrespective of Re values. However, the kinetic energy transport followed a nonlinear dependency on porosity.

A lot has been published and comprehended about how a sheet of liquid or a bubble/droplet ruptures under applied pressure [27–31]. It is well known that a sheet of liquid on rupture results in the formation of a hole that expands at a certain velocity by the action of the surface tension as it reaches the end of the sheet. The speed of retraction was independently given by Taylor [32] and Culick [33]. The liquid that existed at the site of the hole gets concentrated in the rolled-up edge [34], known as the rim. During expansion, this rim remains highly unstable, releasing droplets. The physics of rim destabilization that ultimately leads to the formation of ligament-like structures and droplets has been discussed [28,35–37]. The breakup of a droplet into different stages, including the growth of a bag, bag bursting, fragmentation, ligaments, and droplets, has been reported [29,38–40].

The available literature shows that a limited amount of work has been done on the interaction of vortex rings with porous surfaces. More importantly, researchers have mainly focused on uniform porous screens and laminar vortex rings. In the present study, we investigate the idea of vortical cleaning, which is achieved by letting a vortex ring impinge on oil-laden porous surfaces. Usage of a vortex ring instead of a continuous jet has several advantages, one of which is that a vortex ring has the potential to clean the porous surface from both sides (as will be discussed later) much more

effectively than a continuous jet. Moreover, the generation of vortex rings requires less energy than continuous jets because of their intermittent nature. However, generating a jet is relatively simpler than creating vortex rings. Most industrial filters are cleaned by dismantling them from the main unit; however, by virtue of the vortex ring, filters can be cleaned at their installed sites from both sides. Furthermore, the concept of vortical cleaning can be utilized to clean surgical masks or other soft porous surfaces. The idea of vortical cleaning is novel and hence still in its initial stage. We test the hypothesis and focus on understanding the involved mechanism. We look into the vortex dynamics of the interaction process and the sheet dynamics of the expunged oil by considering two types of porous surfaces made of spherical beads having two different ϕ values (0.21 and 0.41). The interaction process with oil has been divided into three regimes: (i) the penetration regime, (ii) the bag formation regime, and (iii) the bag breakup regime; all three are discussed in detail in the following sections.

The paper is organized as follows: Section II contains details about the experimental setup, Sec. III discusses the results obtained for various cases, i.e., a free vortex ($\phi = 1$), and $\phi = 0, 0.21$, and 0.41 with and without oil, and Sec. IV presents the concluding remarks and a summary of the present work.

II. EXPERIMENTAL SETUP

A. Flow chamber setup

All experiments were conducted inside a water-filled acrylic chamber (250 mm \times 250 mm \times 250 mm) with a free surface of water exposed to the atmosphere, as shown in Fig. 1. The size of the chamber was chosen such that the effects of the wall are negligible. The vortex ring was generated by injecting a fixed volume of water through a pipe of diameter $D = 12$ mm and its axis perpendicular to the plane of the porous surface. The end of the pipe was bevelled at $\sim 10^\circ$ for a smooth roll-up of the shear layer. A solenoid valve connected to an air-pressurized water chamber was used to actuate and control the fluid mass from the injection pipe. The injection pressure was varied from 10 to 50 psi, resulting in the generation of a vortex ring of different strengths. The range of Re_Γ were chosen so as to cover both the laminar and turbulent regimes. For cleaning purposes, interaction with turbulent vortex rings is expected to give better results. The opening time of the solenoid valve was kept constant at 25 ms, controlled by an externally connected Arduino board. An acrylic frame was prepared to hold the porous surface's spherical beads arrangement. The frame was firmly kept at a distance of $5D$ from the injection pipe exit. The usage of acrylic facilitated the optical accessibility required for PLIF and PIV measurements. Initially, the porous surface was placed inside the tank, after which the tank was filled with water. The porous surface was impregnated by injecting the olive oil at desired locations using a handheld syringe. A waiting period of ~ 2 min was observed before every experimental run to achieve the oil film's equilibrium state. The fluid properties and ambient conditions are shown in Table I. The cubical chamber and the vortex ring ejection system were mounted on a heavy-duty X-Y-Z stage (XYZTS series, Holmarc) and rails (HC-2 series, Holmarc) for accurate alignment of the system.

B. Porous surface

A spherical-bead-based porous surface differs significantly from the previously studied surfaces, as discussed in Sec. I. Hrynyuk *et al.* [15] and Naaktgeboren *et al.* [16] used interwoven wires, whereas Adhikari and Lim [14] fused the wires at the junction to avoid an uneven plane. Circular holes were made by the authors of [22,24,25] to fabricate the porous surface. The acrylic frame used for holding spherical beads contains an array of through-holes of size 1 mm separated by a distance of 4 mm. A carbon fiber rod with threaded spherical beads of diameter 3 and 4 mm was firmly fixed in each set of through-holes, forming a porous network [as can be seen in Fig. 1(d)]. As the pitch of the holes on the acrylic frame is fixed, usage of 3- and 4-mm-diam bead sizes results in the formation of uniform and nonuniform porous surfaces (as shown in Fig. 2) with ϕ values of 0.21 and 0.41, respectively. The chosen values of ϕ correspond to relatively lower porosity and

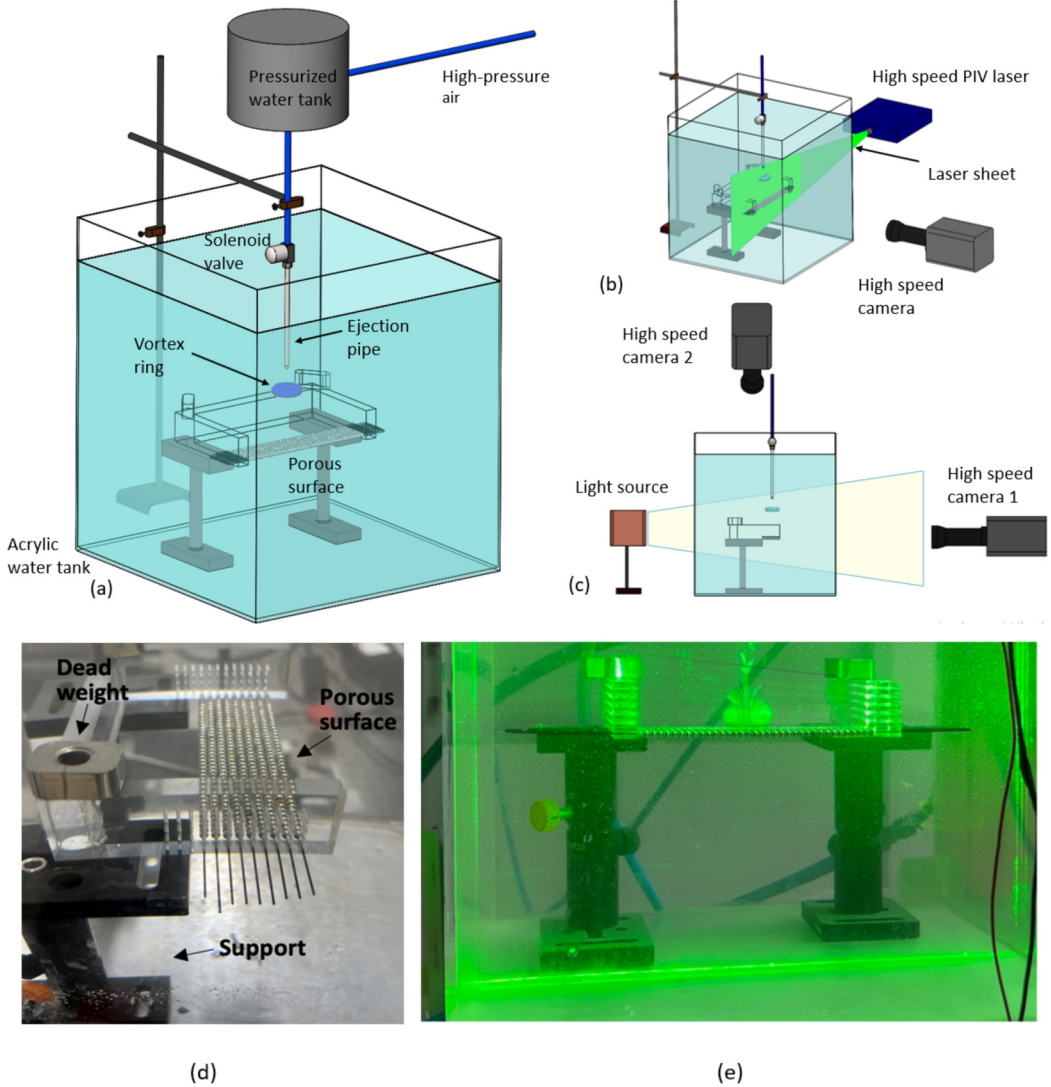


FIG. 1. (a) A typical experimental setup used in the present study. (b) Setup for PIV and PLIF measurements. (c) Setup for shadowgraphy and top view imaging. (d) A nonuniform porous surface placed inside an acrylic water tank. (e) A vortex ring illuminated using a PIV laser just before interacting with a porous surface.

TABLE I. Fluid properties and working conditions relevant to the present study.

S no.	Property	Water	Olive oil
1	Density (ρ : kg m^{-3})	1000	918
2	Viscosity (μ : Pa s)	8.9×10^{-4}	7×10^{-2}
3	Surface tension (σ : N m)	0.012	0.012
4	Ambient temperature $^{\circ}\text{C}$	~ 25	~ 25

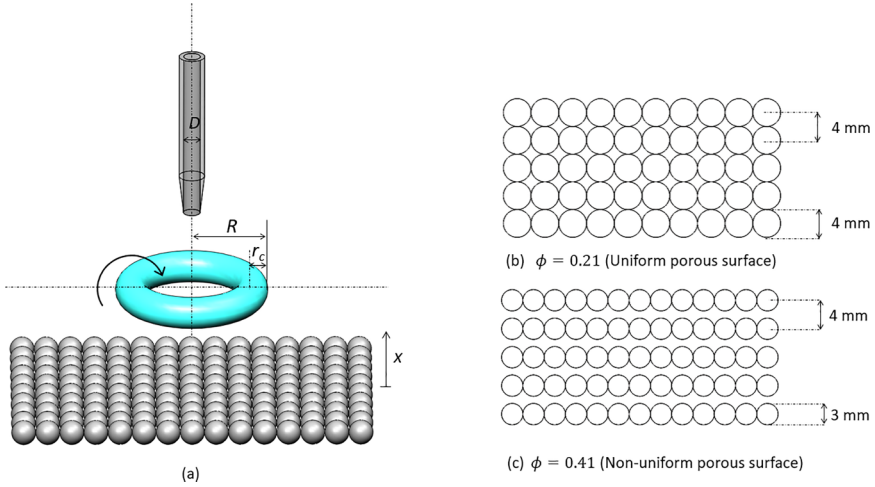


FIG. 2. (a) Schematic showing the important features of a vortex ring. (b) Cross section of the uniform porous surface. (c) Cross section of the nonuniform porous surface used in the present study.

are suitable for testing if vortex rings are capable of cleaning the porous surface at all. Moreover, a nonuniform bead structure mimics a more realistic scenario and has not been investigated before.

C. PIV and PLIF imaging

The PIV measurements were done using a high-speed dual pulse Nd:YLF laser (Photonics Inc., pulse energy of 30 mJ, emission wavelength 527 nm, repetition rate 10 kHz) at a frequency of 1000 Hz. The cylindrical laser beam was expanded and transformed into a planar sheet (~ 1 mm thickness) using a cylindrical lens assembly ($f = -10$ mm), resulting in the uniform illumination of the interaction region [see Fig. 1(b)]. Neutrally buoyant borosilicate glass spheres (Sigma-Aldrich) having a density of 1100 Kg m^{-3} and a mean diameter of $9\text{--}13 \mu\text{m}$ were homogeneously seeded in the vortex and tank fluid. The scattered light from these particles is captured using a high-speed camera (Photron Mini UX) at a pixel resolution of $1280 \text{ pixels} \times 1024 \text{ pixels}$ with a field of view of $63 \text{ mm} \times 52 \text{ mm}$. A duration of $500 \mu\text{s}$ was maintained between two laser pulses to ensure $4\text{--}5$ pixels movement of the seeded particles, necessary for accurate measurement of displacement vectors [41]. All the double frame images were captured and processed in the commercially available PIV software, LAVISION DAVIS 8.4. The images captured during consecutive laser pulses were cross-correlated using multipass processing with decreasing interrogation window sizes. The window size was reduced from $96 \text{ pixels} \times 96 \text{ pixels}$ to $32 \text{ pixels} \times 32 \text{ pixels}$ with an overlap of 75%. More details of the experiments can be found in other works of our group [29,42].

Planar laser-induced fluorescence (PLIF) imaging was done to extract the qualitative information on the morphological changes of the interacting vortex ring. A small amount of fluorescent dye (Rhodamine 6G) was added to the vortex fluid, and the emission light was captured using a high-speed camera (Photron SA5) at an imaging rate of 1000 Hz. Here also, the previously discussed laser sheet arrangement was used for the illuminating region of interest. A pixel resolution of $1280 \text{ pixels} \times 1024 \text{ pixels}$ was used, resulting in a field of view of $63 \text{ mm} \times 52 \text{ mm}$. A band-pass filter of $570 \pm 10 \text{ nm}$ (suitable for the emission range of fluorescent dye) was attached in front of the camera lens (LaVision) that blocked the scattered and stray light from entering the camera sensor.

D. Shadowgraphy and top-view imaging

The side-view shadowgraphs of the interaction phenomenon were captured using a high-speed monochrome camera (Photron SA5) at an imaging rate of 4000 Hz. An LED light source (Zaila light source) and a diffuser plate were placed opposite the camera lens, which uniformly illuminates

TABLE II. Different parameters of the vortex ring and experimental setup used in the present work. Here, P_{in} refers to the injection pressure at which the vortex ring is generated; r_c refers to the core radius; ϵ is the normalized core radius; U_c is the transnational velocity of the vortex core in the axial direction; Re_Γ is the Reynolds number based on circulation; Re_j is the Reynolds number based on the exit velocity of the jet and core radius ($Re_j = \rho U_j D / \nu$; Δt , the time interval between two laser pulses, was kept constant at 500 μ s).

P_{in} (psi)	r_c (cm)	ϵ (r_c/R)	U_c (cm/s)	Re_Γ	Re_j
10	0.218	0.346	11.29	2550	1427
20	0.242	0.351	22.12	6300	1840
30	0.259	0.319	34.08	10640	2720
40	0.254	0.310	46.30	12150	4726
50	0.252	0.291	46.05	14260	5440

the interaction region. The test rig was placed in between the light beam path, as shown in Fig. 1(c). A pixel resolution of 1024 pixels \times 1024 pixels was used, resulting in a field of view of 42 pixels \times 42 pixels. Another high-speed camera (Mini UX100) was operated at an imaging rate of 1000 Hz to capture the top-view images of the interaction phenomenon [see Fig. 1(c)]. Since the top view of the phenomenon is used only for qualitative understanding and visualization, a different imaging rate was considered.

E. Experimental conditions and measurements

All the experiments were done underwater, and the vortex strengths were varied by controlling the fluid injection pressure. For all the cases, the porous surface is kept at a distance of $5D$ from the ejection pipe. The quantitative measurements were done using the vector field data obtained from the PIV experiments. As shown in Fig. 2(a), the core radius (r_c) is defined as half of the distance between the maximum and minimum values of vertical velocities on either side of the vortex core [29]. The ring radius (R) is defined as the distance between the core and ring center. The circulation strength (Γ) of the vortex ring was calculated at a distance of $x \sim 2D$ from the top of the porous surface by taking an area integral of the vorticity (ω) values over the vortex core [29]. The error in the circulation measurement ranges from 1 to 12 $\text{cm}^2 \text{s}^{-1}$. The generated vortex ring in the present study can be classified into a thin vortex on the basis of the nondimensional core radius (ϵ) (see Table II) [43,44]. The noise in the PIV measurements for vorticity was found to be $<50 \text{ (s}^{-1}\text{)}$, which was kept as the thresholding criteria. In calculating kinetic energy and enstrophy of the upstream vortex ring, a MATLAB code was utilized in which a rectangular masking function was defined. For a vortex ring before interaction, the length of the mask was $\sim 3.8R$, and for an interacted vortex ring in the downstream region the mask was created such that it encompasses all the interaction events ($\sim 5R-6R$). A pendant drop method was used for measuring the surface tension of the olive oil–water system using an optical contact angle measuring and contour analysis system (OCA25) instrument from Dataphysics VR. Viscosity measurement of the olive oil was done using a flat plate geometry (plate diameter: 50 mm) of a commercial rheometer (MCR 702, Anton PAAR). The relevant fluid properties for the test fluids are provide in Table I.

III. RESULTS AND DISCUSSION

A. Evolution of free vortex ring

Visualizing the evolving structure of a vortex ring has traditionally been an important tool in deciding its nature [1,45,46]. The case of a propelling free vortex without interacting with any kind of surface serves as a standard case with $\phi = 1$.

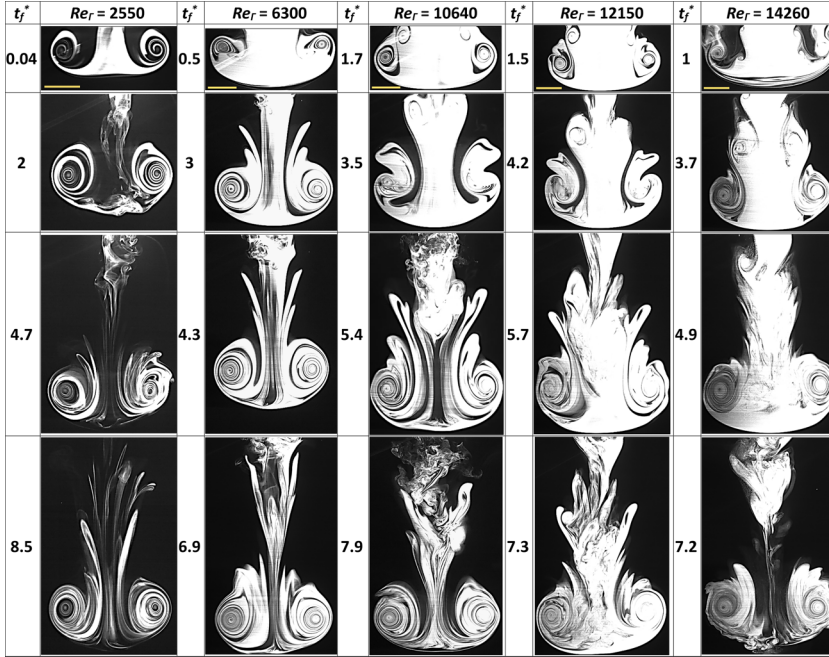


FIG. 3. Evolution of free vortex rings at different Re_Γ shown at different time instances. The initial row depicts the flow structures at the time of ejection, and the final row shows the vortex ring structure near the location of interaction ($x \sim 0.85D$). The scale bar represents 5 mm.

Figure 3 shows the evolution of a free vortex ring for different tested values of Re_Γ before the interaction at different nondimensional time $t_f^* = t_f U_c / r_c$; U_c is the convection speed of the vortex ring and r_c is the core radius. $t_f = 0$ is the instance when the vortex core starts to develop after the fluid is ejected out of the pipe and the final images are captured at $x \sim 0.85D$. Although it is seen in the present study (as will be discussed later) that the incoming vortex ring is affected by the presence of the porous surface, most of the flow structures before interaction remain the same for the free vortex and interaction cases. For the lowest Re_Γ value, the rolling-up process near the injection region is seen to be smooth and a fully developed laminar vortex ring is formed by $t_f^* = 8.5$ having a laminar core and wake. A similar observation can be made for $Re_\Gamma = 6300$, except during the initial roll-up some hints of formation of the secondary vortices can be found (Figs. 3 and 4, $Re_\Gamma = 6300$). For $Re_\Gamma > 6300$, prominent secondary structures in the shear layer similar to what was observed by Gharib *et al.* [10] develop (Fig. 3, $t_f^* = 1.7$ for $Re_\Gamma = 10640$, $t_f^* = 1.5$ for $Re_\Gamma = 12150$, $t_f^* = 1$ for $Re_\Gamma = 14260$) that get consumed in the primary core. Only in the case of $Re_\Gamma = 14260$ can very small-scale shear-layer-induced KH-type vortices be sighted at the edges of the central jet coming out the pipe (at $t_f^* = 1$). In the last frame for cases with $Re_\Gamma > 6300$, the core of the vortex ring can be seen to be well-defined, the wake to be turbulent, and the surface to be rough, confirming that the vortex rings are turbulent [45]. Furthermore, the Re_j values obtained in the present study (see Table II) are much higher than the threshold of 600 observed by Maxworthy [6] for the azimuthal instability to grow.

Velocity vectors blended with vorticity in the background at the time of ejection from the pipe are shown in Fig. 4, where the formation of shear-layer vortices for $Re_\Gamma \geq 6300$ is evident. The shear layer is contained with sharp gradients in velocity compared to a much more stable surrounding fluid, resulting in the rolling up of shear layers. From Figs. 3 and 4 it can be seen that the vortex ring does not lose its symmetricity even at higher values of Re_Γ . From the PLIF and PIV data, it can reasonably be deduced that during the interaction, the trailing jet almost ceases to feed vorticity to

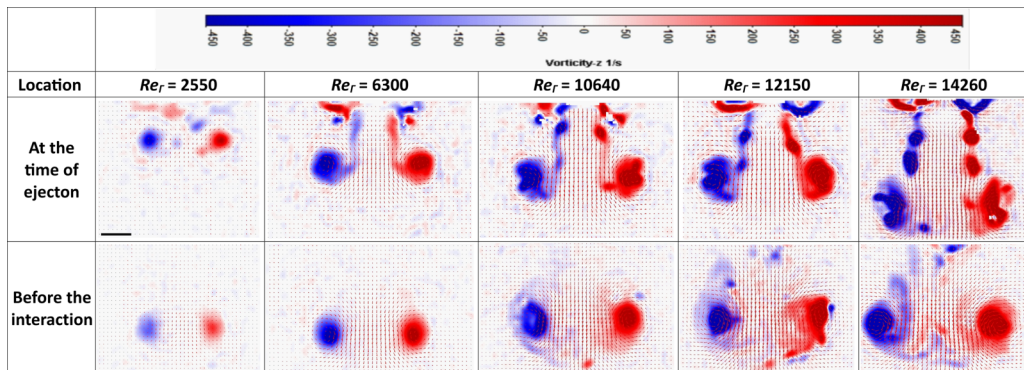


FIG. 4. Vorticity contours at the time of ejection and before interacting at different Re_Γ . The occurrence of shear-layer vortices can be visualized from the first row especially at higher values of Re_Γ . The scale bar represents 5 mm.

the primary core, i.e., the interaction process occurs when the vortex ring becomes fully developed. Additional details about the vortex ring have been listed in Table II.

B. Interaction with $\phi = 0$

The case of $\phi = 0$ represents the other extreme, which involves the interaction of a vortex ring with a plane solid impermeable wall with no slip boundary condition. $\phi = 0$ has been extensively studied before [47–49], as discussed in Sec. I, but it is used here for validation and comparison. Figure 5(a) shows the PLIF images of a vortex ring with $Re_\Gamma = 2550$ propelling towards a solid wall. Here, the nondimensional time (t_w^*) is defined as $t_w^* = t_w U_c / r_c$, where $t_w = 0$ is at $x \sim 0.6D$. The main features of such interaction include the free traveling of the vortex ring, vortex stretching, and vortex rebound [49], which are very well captured. As the vortex ring approaches the wall, it starts to expand radially, and a boundary layer of opposite sense develops at the surface of the wall (Fig. 5). In the region between the leading edge of the vortex ring and the wall, an adverse pressure gradient develops [47] that ultimately leads to the separation of the boundary layer giving rise to a secondary vortex, having an opposite sense of rotation, arrests the radial expansion of the primary core forcing it to rebound. For $Re_\Gamma \geq 10\,640$, the three-dimensional effects dominate after interaction (Fig. 6), resulting in a chaotic rebounding process.

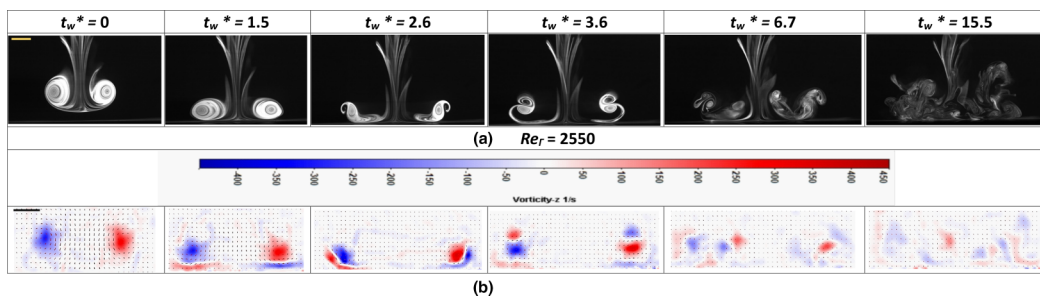


FIG. 5. $\phi = 0$. (a) PLIF, (b) PIV images at $Re_\Gamma = 2550$. The scale bars represent 5 mm. As the vortex ring approaches the solid surface, a series of phenomena including vortex stretching and rebounding can be seen.

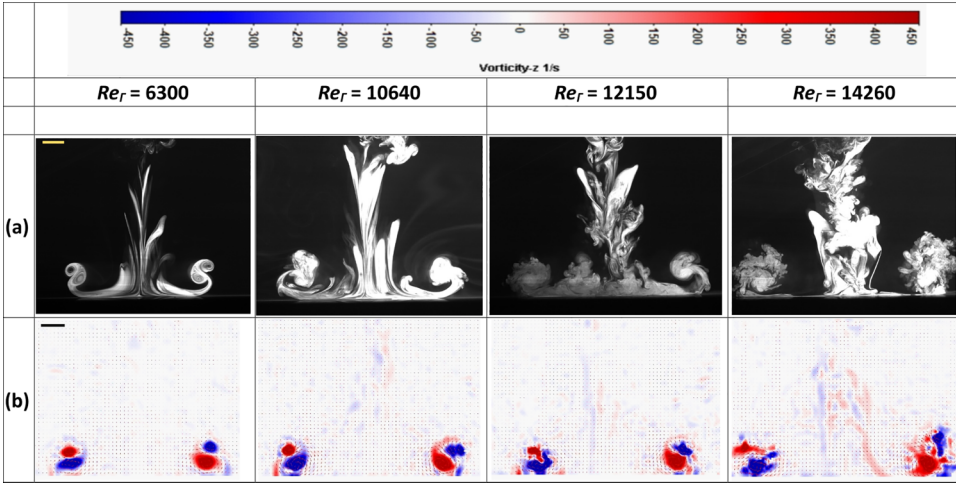


FIG. 6. (a) PLIF, (b) PIV images at different Re_Γ after interaction for $\phi = 0$. The scale bars represent 5 mm. The three-dimensional affects become prominent with an increase in the value of Re_Γ as can be seen from both PLIF and PIV images.

C. Interaction without oil

Here, we look into the physics behind the interaction process without oil. A detailed qualitative (using PLIF data) and quantitative (using PIV data) discussion is provided for both ϕ values.

1. $\phi = 0.21$

Figure 7 shows the PLIF images for the case with $\phi = 0.21$ for different Re_Γ values, and Fig. 8 depicts the vorticity contours with the vector field background obtained from the PIV data for different instances. Images at different nondimensional steps have been shown with t^* ($= tU_c/r_c$) = 0 being the time of first instance when the penetration is detected downstream through the porous surface. It is important to note that the value of Re_Γ or Re_j for most of the past works [14–16,23,26] ranges within the laminar regime itself starting from very low values. However, keeping in mind the application, in the present work the Re_j values are significantly large. Moreover, in none of the previous studies have different shapes of the porous surface been considered. The shape of the hole from which the fluid comes out plays a significant role in deciding the nature of the downstream transmitted flow and the regenerated vortex ring.

On ejection, the vortex ring propagates towards the porous surface at a self-induced velocity and expands radially based on the Biot-Savart law [14,16] prior to interacting with the porous surface with $\phi = 0.21$ (see Fig. 7). This radial expansion is highly dependent on the type of porous surface and its porosity. In the case of $\phi = 0$, it would be maximum, and as we increase the value of ϕ , this radial expansion will decrease [26]. This is because at higher values of ϕ , more fluid is allowed to pass through the holes reducing the upstream mass content at a faster rate. The interaction process becomes highly three-dimensional upstream even for the lowest Re_Γ case. That is why in the PLIF images for $Re_\Gamma = 2550$, the primary vortex after interaction (Fig. 7, at $t^* = 3.9$) becomes chaotic. However, the core at the upstream region can be identified well in the PIV images (Fig. 8). As we increase the Re_Γ , a more disordered upstream region develops, where a boundary layer of opposite sense rolls up into the formation of a secondary vortex similar to what is observed in cases with $\phi = 0$. This can be visualized with the PIV data for all the cases at the initial instance (Fig. 8). The boundary layer that developed gets pulled up by the shearing action of the primary core, thereby restricting its radial expansion. However, the coherency of the secondary vortex ring is lost during this interaction for all the cases.

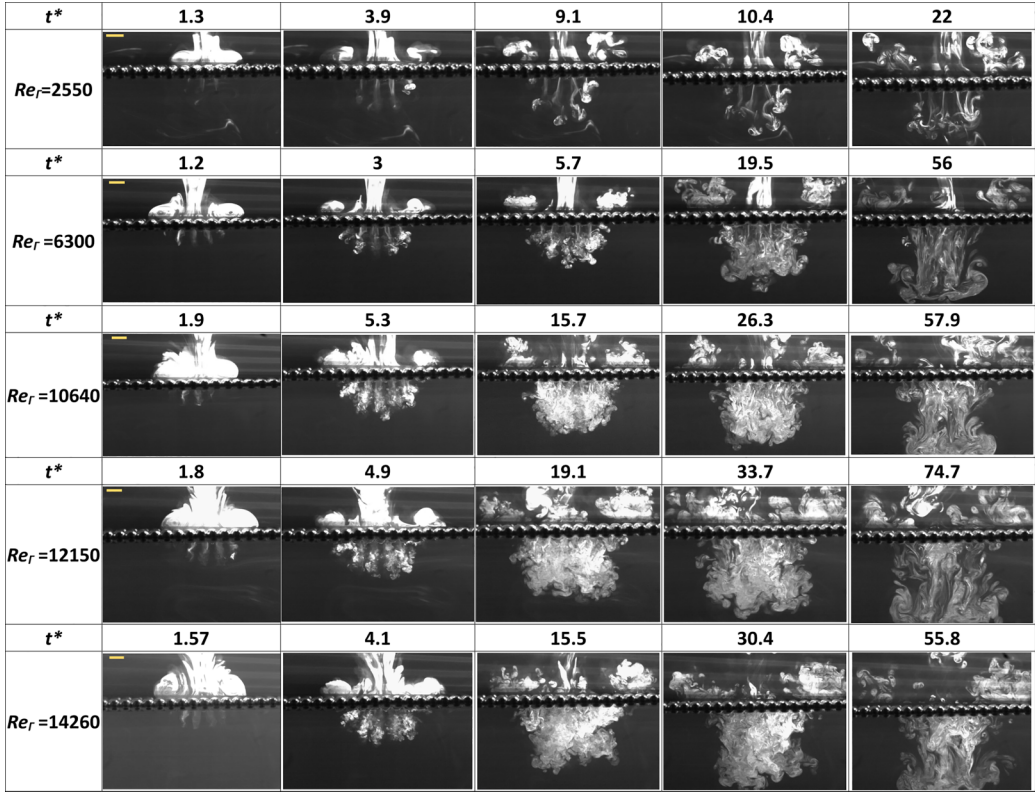


FIG. 7. PLIF images for $\phi = 0.21$ with no oil at different values of Re_T shown at various t^* . The scale represents 5 mm for each Re_T value.

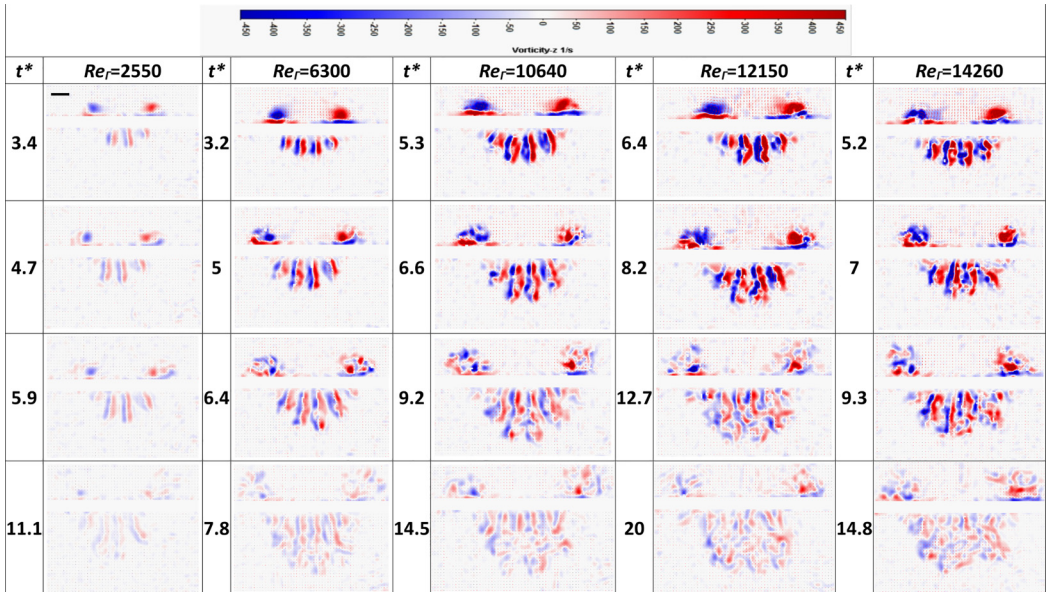


FIG. 8. PIV images for $\phi = 0.21$ with no oil at different values of Re_T shown at various t^* . The scale bar represents 5 mm.

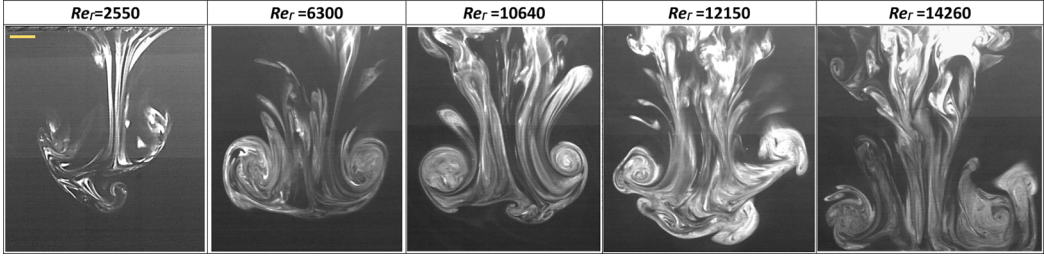


FIG. 9. PLIF images of vortex reformation in the downstream region for $\phi = 0.21$ with no oil at different Re_Γ . The scale bar represents 5 mm.

In the downstream region, due to the shape of the hole for $\phi = 0.21$, the fluid initially comes out as small individual jets from each hole containing vorticity. For $Re_\Gamma = 2550$, these jets propagate a long distance downstream before interacting with each other. At $t^* = 9.1$ (Fig. 7, $Re_\Gamma = 2550$), we can see that the head of each jet develops a small-scale vortex ring that, due to the instability, cannot remain in a straight path and ultimately interacts with neighboring small-scale rings. The concept of vorticity cancellation as has been discussed before [14,16] can be applied here to understand the phenomenon. From the PIV data (Fig. 8), it is clear that the jets carry vorticity of opposite sense as they emerge out of the holes for all the cases. The gap between two jets being sufficiently large does not allow the cancellation of vorticity for $Re_\Gamma = 2550$ where the jets develop individually for a large distance. For other cases, the jets coming out of the hole carry a lot of kinetic energy, and the individual jets as they pass through the holes lose their order in a three-dimensional manner. This is supported by the PIV data, where we can see that with the increase in Re_Γ , the mixing becomes more prominent over time. The possession of high velocity triggers KH-type instabilities [22,26] in the jets resulting in numerous small-scale features and a highly complex vortex cancellation process. This cancellation ultimately results in the regeneration of a vortex ring downstream [14]. The effect of the velocity distribution before interaction (i.e., more at the center of the flow field) is propagated downstream as well, and hence the flow in the central region has more kinetic energy compared to the distant fluid (see Fig. S1 [50] and supplementary movie 1-4 [50]). This difference in the bulk motion between the center line fluid and the distant fluid ultimately leads to the formation of the coherent regenerated vortex ring downstream. The core of this regenerated vortex has multiple small-scale features due to jet interaction across planes, KH instability, and the vortex cancellation. For $Re_\Gamma = 2550$, the regenerated vortex ring only partially reformed, and no coherent structure was observed because of the diffusion of the flow (see Fig. 9). In other cases, it had lost most of its strength, but the structure could be visualized using the PLIF technique. For $Re_\Gamma = 6300$ and 10 640, a clear regenerated vortex ring can be observed at $\sim 2.7D$ (the core visualized with eye from Fig. 9) measured from the bottom surface of the beads. For $Re_\Gamma = 12\ 150$ and 14 260 the distance was $\sim 3.3D$ and $\sim 3.7D$, respectively.

2. $\phi = 0.41$

The interaction of a vortex ring with a nonuniform porous surface ($\phi = 0.41$) reveals different flow features. Figure 10 shows the PLIF images at different instances, and Fig. 11 depicts the PIV data showing the contours of the vorticity and velocity vectors. Due to the increase in ϕ , in the upstream, the vortex core evolves differently during the interaction. The overall radial spread of the vortex ring on impinging reduces considerably with a short-lasting boundary layer. The rebound of the vortex core weakens due to the large hole size. A weaker secondary vortex develops for all the cases (see Fig. 11) that tries to push the main core, making it penetrate through the porous surface instead of rebounding. The difference in the upstream dynamics can be clearly visualized from the PIV data of uniform and nonuniform surface interactions (Figs. 8 and 11). In the case of a uniform

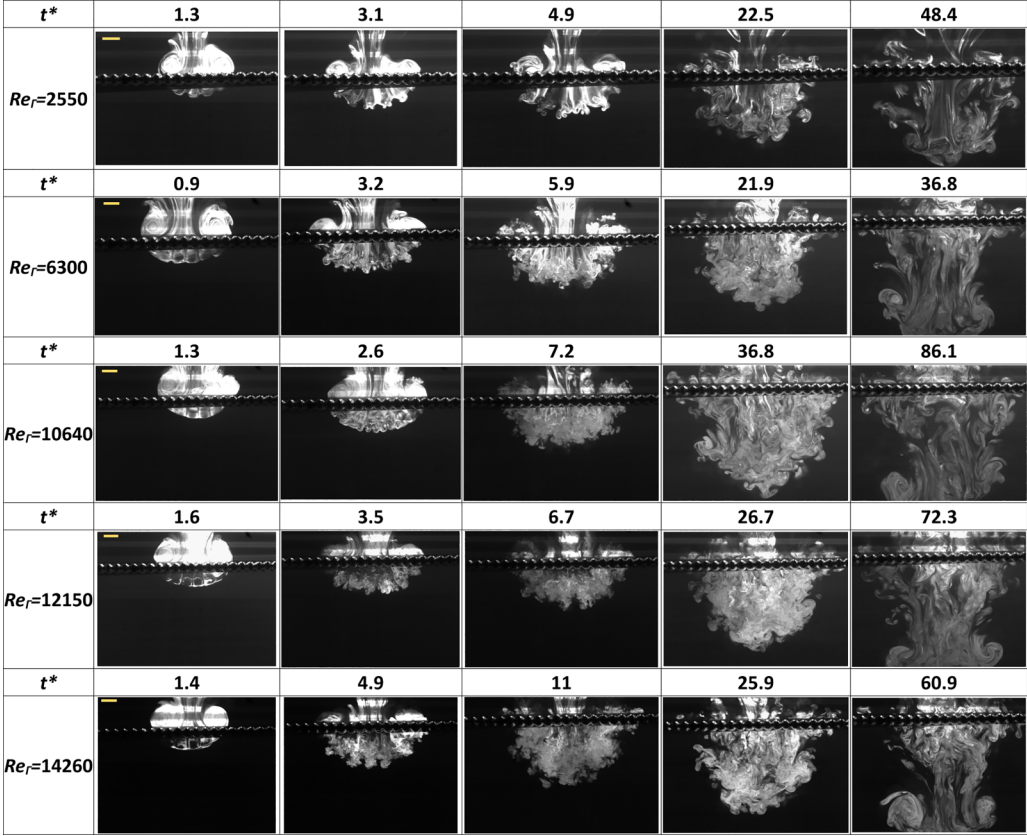


FIG. 10. PLIF images for $\phi = 0.41$ with no oil at different values of Re_Γ shown at various t^* . The scale represents 5 mm for each Re_Γ value.

surface ($\phi = 0.21$), the upstream fluid has considerable vorticity even until the last time instance shown here for $Re_\Gamma \geq 6300$, which is not the case with $\phi = 0.41$.

The fluid in the case of $\phi = 0.41$ comes out as a sheet instead of individual small-scale jets. As can be seen in the first instance for all the cases (Fig. 10), a corrugated shaped sheet of fluid comes out of the porous surface that weakens in amplitude with an increase in Re_Γ . The corrugation is the result of the shape of the hole for $\phi = 0.41$. The corrugation flattens because at higher Re_Γ values, the flow passing through the hole is able to overcome the drag due to the beads, thereby reducing its effects. As time increases for $Re_\Gamma = 2550$, the head of the corrugation becomes unstable and starts to form small-scale mushroom-shaped features ($t^* = 3.1$, Fig. 10). The structure is 2D in nature and evolves until they are disturbed ($t^* = 4.9$) by the developing adjacent structures. Here, in the PLIF images for $\phi = 0.41$ we focused on the events occurring in the plane of the central hole in the porous surface. But for $\phi = 0.41$, it was seen that the vortex ring comes out of three such holes [see Fig. 2(b), showing the cross section of the porous surfaces]. The disturbance propagates in all directions, resulting in the culmination of small-scale structures into larger ones. For $Re_\Gamma = 6300$, the sheet can be seen to be uniform initially ($t^* = 0.9$), but then loses its uniformity in the form of small-scale vortices at the head (Fig. 10, $t^* = 3.2$). Similarly for $Re_\Gamma = 10640$ at $t^* = 2.6$ (Fig. 10), a more chaotic sheet is observed followed by mushroom structures at the end of the sheet. The flow develops into an extremely disordered pattern over time with the central part of the bulk flow ahead of the distant ones. For $Re_\Gamma = 12150$ and 14260 , the mixing of flow starts very early due to the KH instability and the instability triggered by the corrugated shape. The water sheet coming out

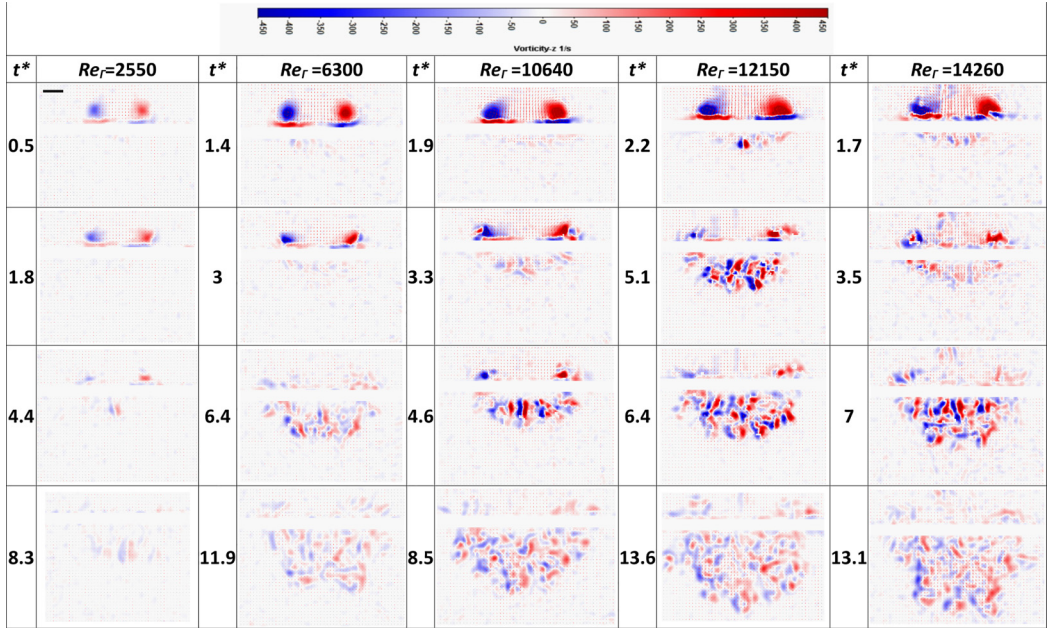


FIG. 11. PIV images for $\phi = 0.41$ with no oil at different values of Re_T shown at various t^* . The scale bar represents 5 mm.

of the porous surface has a relatively higher velocity than the quiescent water in the surrounding of the flow resulting in the growth of KH instability. The vorticity cancellation effectively occurs in a direction perpendicular to the page resulting in the formation of the regenerated vortex ring (Fig. 12). The PIV data (Fig. 11) further confirm that the flow spreads over a larger area with more small-scale mixing in this case compared to the uniform porous surface. The regenerated vortex ring is more disorganized compared to $\phi = 0.21$. For the initial Re_T value, the vortex ring could not be reformed, as also seen previously. For Re_T 6300 and 10 640 the vortex ring reformed at $\sim 3D$ and $\sim 3.4D$ (Fig. 12). For the other two cases, the regenerated vortex ring formed much below the capturing frame and could not be shown here. Compared to $\phi = 0.21$, the regenerated vortex ring observed for $\phi = 0.41$ has much more smaller-scale features mostly at the central region. Due to the flow being much more three-dimensional here, the small scales do not dissipate. The reason for the vortex regeneration remains the same as for the previous case, i.e., higher velocity at the central region (see supplemental Fig. S2 [50]). Compared to $\phi = 0.21$, the flow downstream for $\phi = 0.41$ has much more kinetic energy, as can be seen in Fig. S2 [50]. The strength of the regenerated ring

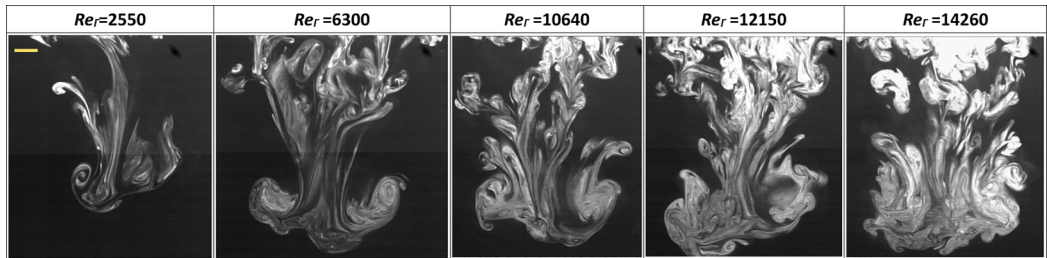


FIG. 12. PLIF images of vortex reformation in the downstream region for $\phi = 0.41$ with no oil at different Re_T . The scale bar represents 5 mm.

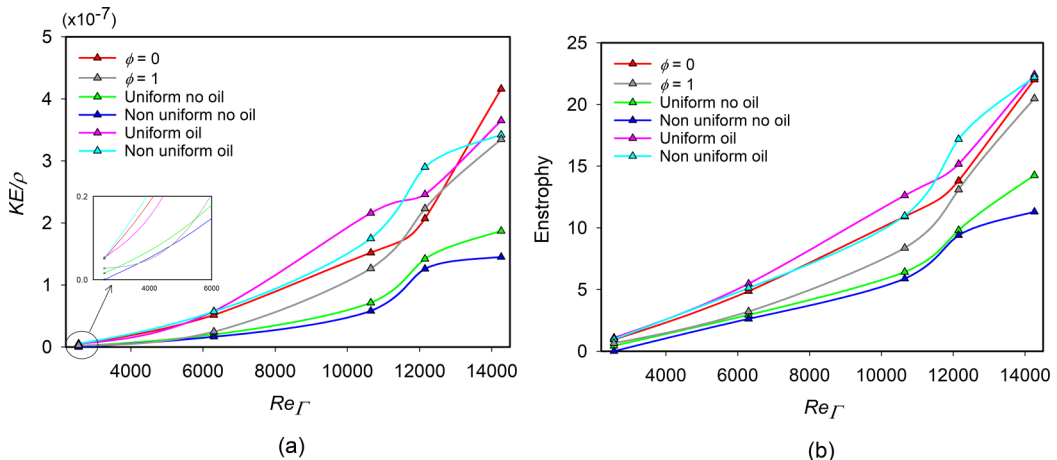


FIG. 13. (a) Kinetic energy (inset shows the KE/ρ values for $Re_\Gamma = 2550$). (b) Enstrophy of the upstream vortex ring at $x \sim 1.5D$.

was found to be extremely low, so that it almost matched with the surrounding noise in the data (not shown here).

D. Interaction with oil

In this section, we first explore the effect of placing the porous surface with and without oil on the incoming vortex ring. Further, the interaction phenomenon will be discussed, which is divided into three regimes: (i) penetration, (ii) bag formation, and (iii) bag breakup. Along with PLIF and PIV techniques, high-speed shadowgraphy images will be utilized to understand the phenomenon.

1. Effect of porous surface on the incoming vortex ring

The PIV data are utilized to calculate the kinetic energy (KE) and the enstrophy of the incoming vortex using the following formula in their dimensional forms:

$$KE/\rho_w = \int (u^2 + v^2) d\mathcal{V}, \quad (1)$$

$$\text{Enstrophy} = \int (\omega^2) d\mathcal{V}, \quad (2)$$

where \mathcal{V} is the volume of interest. For axisymmetric conditions, we calculate the area integral for both the kinetic energy and enstrophy. Figure 13 shows the trend of kinetic energy and enstrophy at different Re_Γ values for all six cases including $\phi = 0$ and 1. These data have been plotted at $x \sim 1.5D$. It can be clearly seen that the kinetic energy values of the free vortex are different from other cases and lie between the oil and no-oil cases. As expected, the values of both kinetic energy and enstrophy increase as we go on increasing Re_Γ . It is crucial to note that the cases with oil behave almost like the case having $\phi = 0$. Since the ϕ of the two porous surfaces does not differ by a huge margin, the effect of ϕ on the incoming vortex ring is much less, hence it has been ignored in the present study. Although the difference becomes significant in the higher Re_Γ regime, in the interest of our ultimate goal, we ignore this difference. But for oil-laden porous surfaces, the incoming vortex ring senses the porous surface as a flexible wall in its path of propagation. A similar trend is followed by the enstrophy of the vortex ring. Figure 14 depicts the trajectory of the vortex core for one-half of the vortex ring for different interaction conditions at different Re_Γ . The y axis is merged with the center line of the vortex ring that corresponds to the axial distance, and

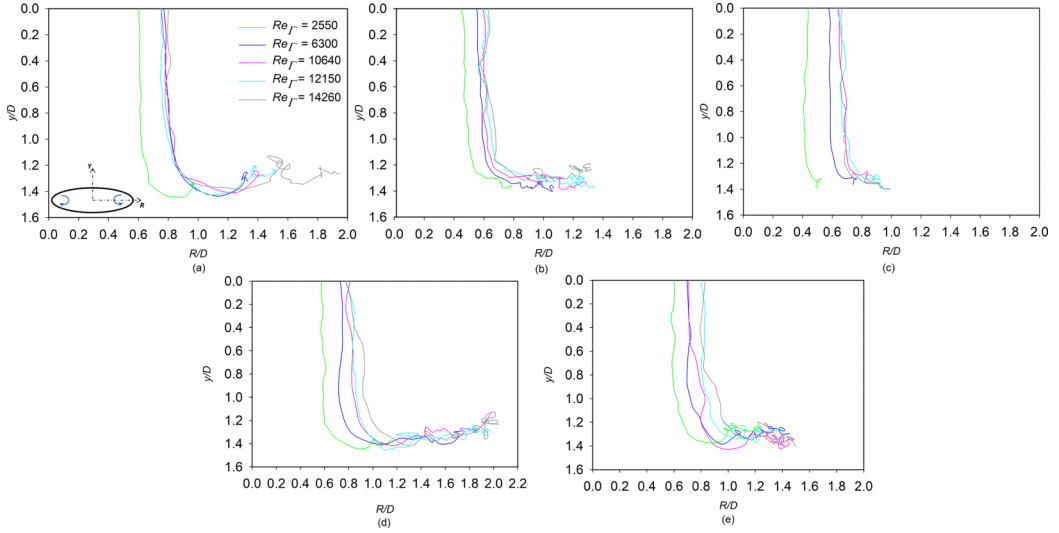


FIG. 14. Vortex core trajectory for (a) $\phi = 0$, (b) uniform ($\phi = 0.21$) no oil, (c) nonuniform ($\phi = 0.41$) no oil, (d) uniform ($\phi = 0.21$) oil, and (e) nonuniform ($\phi = 0.41$) oil at different Re_Γ values.

the x -axis indicates R . For $\phi = 0$ and $Re_\Gamma \leq 10640$ the core exhibits a single rebound, whereas multiple rebounds are seen for higher Re_Γ . It is interesting to note the distance traveled by the core from the center line in the horizontal direction. The vortex core at higher Re_Γ values deviates the maximum near $y/D = 1$ for cases having oil compared to cases with lower Re_Γ and no-oil cases. For the nonuniform no-oil case, the distance traveled by the core is less even at the same Re_Γ compared to $\phi = 0$ because of the porosity that lets the core pass out faster. The trajectory for all the cases remains disordered, consisting of sharp turns. It should be noted that very small rebounds may not get captured while tracking the core and may look like sharp points. For cases with oil, the core trajectory after interacting becomes more random with multiple rebounds. These cases [Figs. 14(d) and 14(e)] show similar features as seen for $\phi = 0$. The core in the upstream region can be modeled as if it is interacting with an impermeable surface. Additionally, the trajectory gives important information about the region from which the oil can be extracted. In a sense, it tells us about the radial reach of a vortex ring in extracting the trapped oil from the upstream region. This information can be used to find the upstream cleaning efficiency of the vortex rings.

Figure 15 shows the trend in which the kinetic energy of the upstream vortex ring dissipates. Understanding this is important due to the extraction of a significant amount of oil from the upstream interaction (which will be discussed in Sec. III D 5). The $t_k^* (= t_k U_c / r_c) = 0$ instance is assumed at $x \sim 0.5D$. The kinetic-energy data are normalized with the initial value to depict the dissipation rate. Two important factors that need to be considered while understanding how the kinetic energy gets dissipated in the upstream region are the ϕ and the presence of oil. The fate of the upstream vortex ring energy can be decided whether by dissipation via interaction with the surface, interaction with oil, or simply by passing through the porous surface. For a lower ϕ value, less fluid is allowed through the porous surface, resulting in more accumulation of upstream energy [17]. This energy then dissipates with time due to the viscous interactions between the porous surface and the fluid. This argument is valid for laminar cases without oil ($Re_\Gamma = 2550$), where we can see that the uniform no-oil case has a lesser dissipation rate compared to the nonuniform oil case. However, as we move towards a turbulent regime, the trend tends to reverse after a specific t_k^* . For example, at $Re_\Gamma = 12150$ until $t_k^* \sim 3.3$ (Fig. 15), the energy dissipation occurs faster in the uniform no-oil case, after which it occurs in the nonuniform no-oil case. This is because initially when the vortex ring just touches the upper surface, the viscous dissipation occurs faster for a lower ϕ value (i.e., a

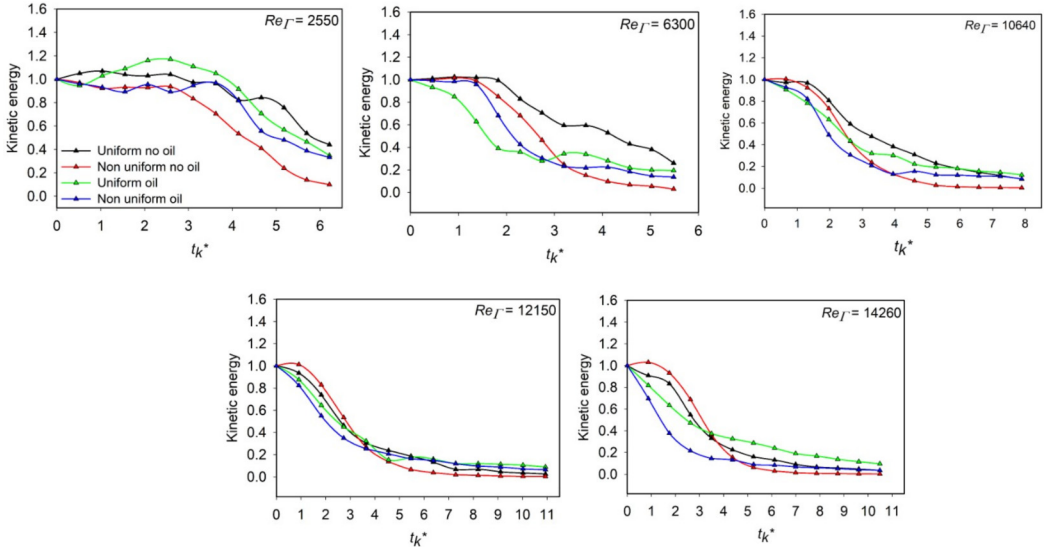


FIG. 15. Upstream energy dissipation at different Re_Γ for different types of porous surfaces with and without oil. The kinetic energy shown here is normalized by the initial kinetic energy of the vortex ring.

uniform porous surface) with a higher surface area for interaction at the upstream surface. But as the interaction progresses, more energy is allowed to pass through the higher ϕ value surface, resulting in faster dissipation after a certain time.

For cases with oil, the lowest value of Re_Γ shows a different behavior where the energy value goes above 1 erroneously. For other Re_Γ values, we initially see faster dissipation in uniform cases for $Re_\Gamma = 6300$ and 10640 . With the increase in the Re_Γ values, the trend interchanges and the intersecting t_k^* point moves slowly towards the left in the graph. As the Re_Γ increases, the vortex ring starts to pass through the porous surface (more in the case of the nonuniform porous surface) and less dissipation occurs due to interaction with the surface. The rate at which the vortex ring passes through the porous surface is fastest for higher Re_Γ values, and hence we see an opposite trend at $Re_\Gamma = 12150$ and 14260 . The reversal at specific t_k^* values is a result of the change in the dominant factor between the ϕ and Re_Γ values. When oil comes into the picture, it gets sheared off by the vortex ring in the upstream region, as will be discussed in Sec. III D 5, which can also change the dissipation rate. The process discussed here depends nonlinearly on many factors, such as the surface area for interaction at the top surface, ϕ , and the presence of oil, resulting in a complex phenomenon.

2. Flow visualization

The PLIF technique (Fig. 16) is used to extract the qualitative information for the interaction of a vortex ring with a porous surface ($\phi = 0.21$) impregnated with oil. The fluid coming out of the porous surface can be visualized at the initial t^* values. We define t^* from the instance when the first penetration is detected downstream through the porous surface, as mentioned in Sec. III C 1. For cases with $Re_\Gamma \leq 6300$, although the oil did not come out of the porous surface, the oil layer inside the oil was perturbed and the motion of the oil layer inside the porous surface was visible. The first instance of visible motion was considered as $t^* = 0$. This referencing is roughly same as what has been done for other interacting cases. For $Re_\Gamma \leq 6300$ (Fig. 16), the vortex ring does not penetrate the surface, and events similar to $\phi = 0$ are observed. As we increase the Re_Γ , the vortex ring penetrates through the hole, stretching the oil in the axial direction and ultimately rupturing it. The ejected fluid carries a lot of circulation that results in the curling of its head, forming small

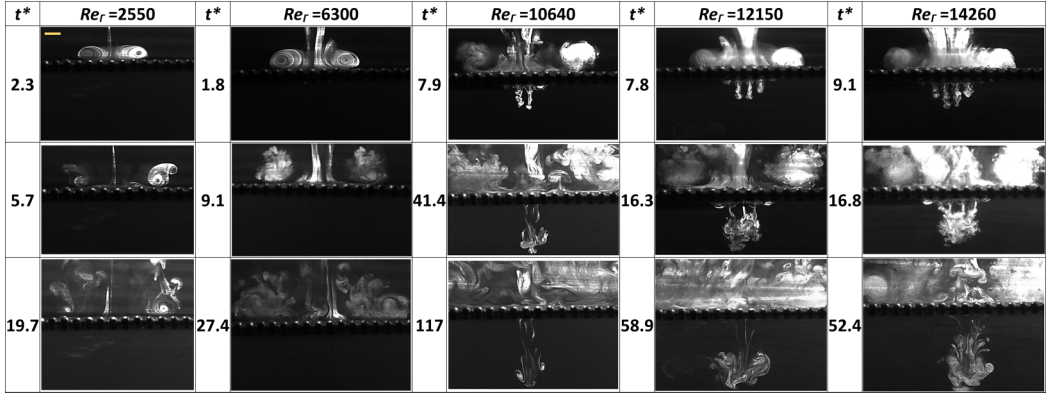


FIG. 16. PLIF images for $\phi = 0.21$ with oil at different values of Re_Γ shown at various t^* . The scale bar represents 5 mm.

mushroom structures. They further interact to create a large-scale transmitted vortex. These flow features were discussed in detail for cases without oil. For the nonuniform porous surface case ($\phi = 0.41$), the vortex ring emerges out of the porous surface at $Re_\Gamma = 6300$, however it is unable to rupture it (see Fig. 17). Due to sufficient surface tension of the oil, the flow is pushed back upward along the central axis (Fig. 17, $t^* = 26.9$), creating intense mixing of the flow upstream. A bag of oil is formed for $Re_\Gamma \geq 10640$, which extends until a certain distance before rupturing. This phenomenon will be discussed in more detail in later sections. Only in cases with high Re_Γ does very weak vortex reformation take place for both porous surfaces in the downstream (not shown here). Introducing oil makes the flow field a multifluid system where PIV data can lead to erroneous interpretations, hence they are not considered here.

3. Penetration regime

To clean the porous surface, the vortex ring needs to penetrate, expunge the oil, and rupture the protruding oil bag. Initially, the oil layer inside the porous surface stays in a perfect equilibrium condition indicating that no net force acts on it. The forces acting on the volume of oil are

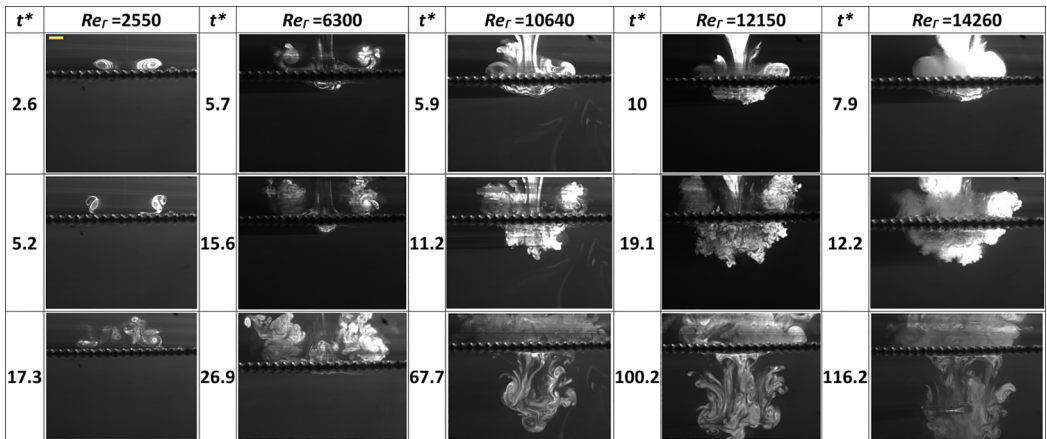


FIG. 17. PLIF images for $\phi = 0.41$ with oil at different values of Re_Γ shown at various t^* . The scale bar represents 5 mm.

the constant buoyancy force and the surface tension forces that cancel everywhere to maintain a balanced scenario. So, theoretically, even the slightest perturbation should cause the mass of the oil to move. However, the critical question here is whether our experimental equipment can detect such slight motion in the oil. Even a little movement in the oil layer indicates that the vortex ring penetrates inside by a certain amount. But, our motive of vortical cleaning is not achieved with it as we want it to push out the oil from the downstream and successfully break it. Here, we define penetration as when the oil layer starts to be visible up to a small distance (half of the bead diameter). We predict the value of the dominating leading term in the second-order fitted trend of distance traveled (h) by the oil at the center line with time in this regime using the Navier-Stokes (NS) equation for a nonuniform porous surface with ($\phi = 0.41$). The bag of oil coming out of the porous surface at the middle plane along the center line is tracked using shadowgraphy images and used to validate the predicted data. The shadowgraphy images give a three-dimensional idea of the interaction that makes it difficult to identify the bag of oil ejected at the center line for the uniform porous surface, hence it has not been considered here. We have the NS momentum equation as

$$\frac{\partial \vec{V}}{\partial t} + \vec{V} \cdot \nabla \vec{V} = -\frac{\nabla P}{\rho} + \nu \nabla^2 \vec{V}. \quad (3)$$

In the penetration regime as defined above, the fluid just starts to move from an equilibrium position, so the convective term of acceleration can be safely neglected. Furthermore, the viscosity term would become dominant only after the penetration regime as the motion considered in this regime is very small. In the period of penetration analysis, the variation in curvature of trapped oil film is almost negligible, hence the surface tension forces are not considered here. By neglecting the less dominant terms, we get a balance between the temporal term and the pressure gradient term as

$$\frac{\partial \vec{V}}{\partial t} \sim \frac{\nabla P}{\rho}, \quad (4)$$

$$a \sim \frac{d^2 h}{dt^2} \sim \frac{1/2 \rho_w V_{in}^2}{\rho_o D_b}, \quad (5)$$

$$h \sim \frac{1/2 \rho_w V_{in}^2}{\rho_o D_b} t^2 = C \frac{1/2 \rho_w V_{in}^2}{\rho_o D_b} t^2, \quad (6)$$

where ρ_w is the density of water, ρ_o is the density of oil, V_{in} is the velocity induced in the flow field along the center line at the point from where the vortex core starts to expand radially, and D_b is the diameter or thickness of the bead. The term on the left side represents the acceleration that has been cast in terms of h . The ∇P is scaled with the dynamic pressure.

Figure 18 shows the variation of h with time in the penetration regime. We can see that for all the values of Re_Γ (≥ 6300), the data obtained show an excellent fit. Figure 18(e) shows the comparison between the predicted coefficient of t^2 and the actual values obtained from experiments. For more robust validation of the prediction, a wider range of Re_Γ is considered here. Almost for all the cases, the coefficient is predicted with a minimal margin of error. The value of the constant C turns out to be ~ 0.48 – 0.5 for different cases. This trend deviates slightly at the higher Re_Γ values where the vortex ring becomes turbulent. Furthermore, all the plots could not be plotted in a single graph as the measurements for h could not be obtained from a uniform starting or ending point for each case. From the comparison obtained in Fig. 18(e), it can be safely concluded that in the penetrating regime, the viscous and other forces like surface tension can be neglected, and the movement of the oil layer can be predicted using scales obtained in Eq. (6).

4. Bag formation

Figures 19 and 21 show the shadowgraphy images for uniform ($Re_\Gamma \geq 10\,640$) and nonuniform porous surfaces ($Re_\Gamma \geq 6300$), respectively. After penetrating, the major forces acting on the system include the inertia forces, viscous forces, and surface tension forces. As the fluid enters through the

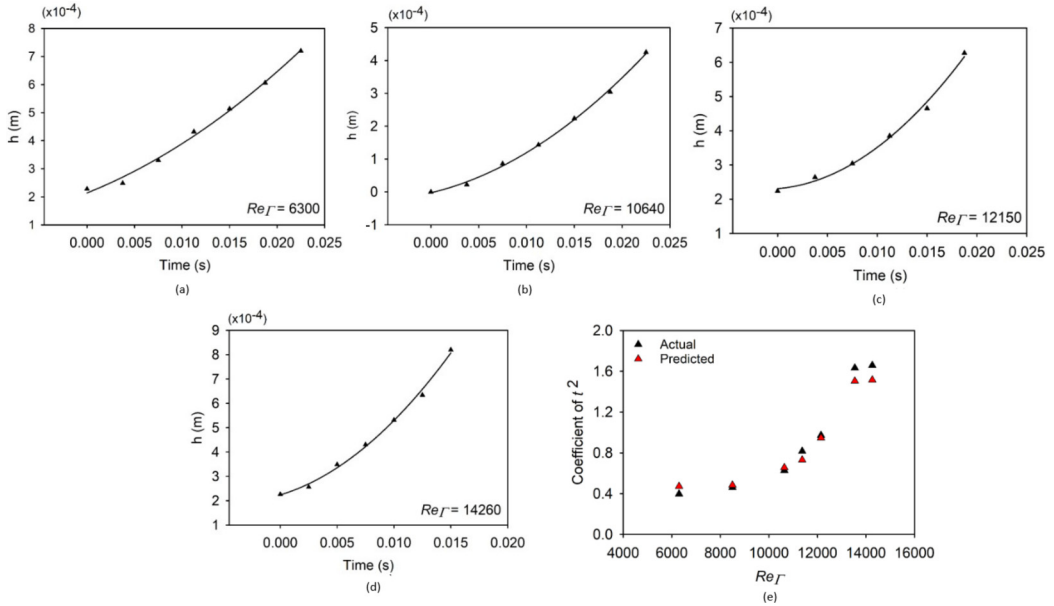


FIG. 18. Variation of h with time at (a) $Re_\Gamma = 6300$, (b) $Re_\Gamma = 10640$, (c) $Re_\Gamma = 12150$, (d) $Re_\Gamma = 14260$, and (e) actual and predicted coefficient of t^2 .

holes, overcoming the pressure force needed to pass through it, it experiences a local increase in its velocity. This inertia force pushes the oil through the porous surface, forcing the oil to stretch downstream. For the uniform porous surface ($\phi = 0.21$), the vortex ring tries to push the oil through each of the holes, making numerous (~ 10 – 12) cylindrical bags of oil with hemispherical ends (see Fig. 19). The ends of the oil layer stay intact at the edges of the bead, resulting in the formation of a baglike structure that continuously gets filled with water until the rupture. With an increase in the

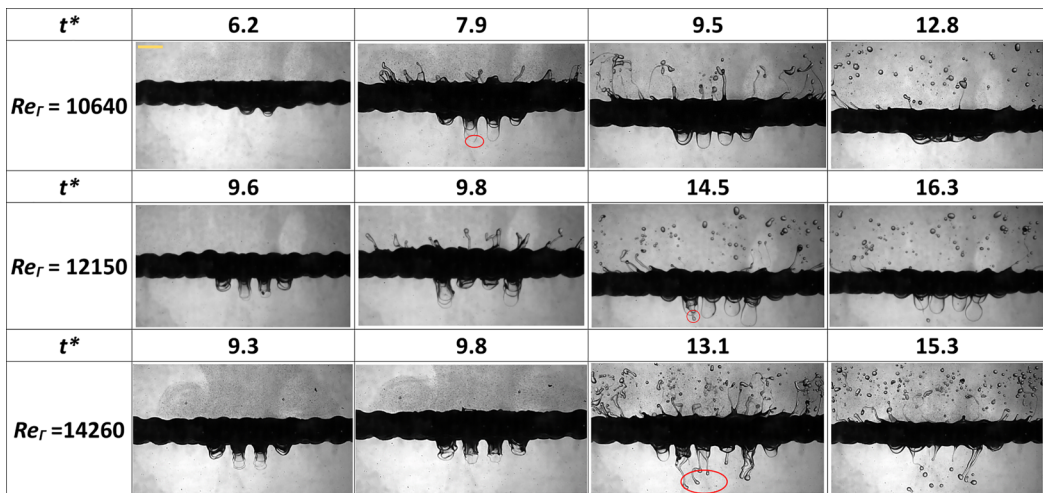


FIG. 19. Shadowgraphy images for $\phi = 0.21$ with oil at different Re_Γ shown at various t^* . The scale represents 5 mm. The marked zone for $Re_\Gamma = 10640$ shows the occurrence of a hole at the head of the cylindrical oil bag. For $Re_\Gamma = 12150$ and 14260 , it highlights the formation of oil ligaments.

Re_Γ value, the radius and strength of the vortex ring also increase, resulting in a larger number of oil bags. The three-dimensional feature in the images can be clearly observed where simultaneous rupturing and formation of a bag can be seen (Fig. 19, $Re_\Gamma = 10\,640$, $t^* = 7.9$; $Re_\Gamma = 12\,150$, $t^* = 9.8$; and $Re_\Gamma = 14\,260$, $t^* = 13.2, 14.5$).

For a nonuniform porous surface (Fig. 21), the vortex rings thrust the oil through the channel-type hole, resulting in the formation of large bags of oil. For all the Re_Γ (except for 2550), three bags of oil are seen. The horizontal expansion of these bags increases slightly with an increase in Re_Γ . For $Re_\Gamma = 6300$ at $t^* = 11.6$, it can be seen that three different types of bag emerge from the porous surface. The central bag has a uniform semiellipsoidal shape that stretches the maximum. The front bag does not show a uniform structure that ultimately gets pulled up. The bag at the back just shows some corrugated structure before being sucked up again due to the surface tension force. The reason for the formation of three different types of bags is the unequal distribution of the vortex ring over the porous surface. The formation of a bag is much more uniform for other Re_Γ because as seen in cases without oil, for lower Re_Γ , the shape of the beads has a profound effect on the flow structure coming out. Similar dynamics occur where the inertia force plays against the resistive surface tension force with a dissipating viscous force acting during the oil motion. As the vortex ring pushes the oil layer, a thin bag having a shape similar to a semiellipsoid starts developing. The incoming water from the vortex ring keeps filling the bag until the surface tension force can withstand the inertia force. The bag formation process becomes more nonuniform as the Re_Γ increases. This is reasonable as we saw in cases without oil that at higher Re_Γ values, the outgoing vortex ring consists of multiple small-scale instabilities.

5. Bag breakup

For $\phi = 0.21$ at $Re_\Gamma = 10\,640$, a bag of oil can be seen to develop a hole at its head that is marked in Fig. 19 at $t^* = 7.9$. This hole forms as a result of continuous thinning of the oil layer that is pushed out of the porous surface. At a certain time, when the oil layer becomes sufficiently small, the layer ruptures. The mass of the fluid that previously occupied the hole site travels immediately to the rim region. Due to the continuous pull generated by the surface tension force, the rim is retracted back to meet the oil sheet at the beads. For higher Re_Γ (Fig. 19, $Re_\Gamma = 12\,150$, $t^* = 14.5$), we can see the formation of ligaments (marked red) due to Rayleigh-Taylor instability [51,52] from the unstable rim that eventually sheds off droplets because of the Rayleigh-Plateau-type instability [51,52]. This is more evident for the highest Re_Γ value (marked red at $t^* = 24.2$). One of the most important aspects of the vortical cleaning seen in the present study is that the oil is taken out by the vortex ring from both sides of the porous surface, as is evident from the shadowgraphy images and top-view imaging (presented supplemental movies 5–8 [50]). This would not be achieved if, instead of vortex rings, water jets were used. For instance at $t^* = 9.5$ (Fig. 19, $Re_\Gamma = 10\,640$), on the upstream side, a large number of oil ligaments form that are curled inwards following the motion of a vortex ring after interaction. These ligaments are stretched in length before they collapse into droplets. Droplet formation from a fluid ligament occurs when the length of the ligament reaches π times its diameter [52,53], but because of the curling, it is difficult to calculate the exact lengths of the ligaments.

The external environment at the time of droplet pinch-off in the upstream region is rotational in nature. Moreover, a pressure variation exists from the outer part of the vortex ring core to its inner part, as suggested by Sharma *et al.* [29]. The lower pressure at the central region of the vortex ring facilitates the rotational motion of the expunged upstream oil. The process of final droplet pinch-off does not occur in a unique way (see supplemental movies 9 and 10 [50] and marked zones in Fig. 20). For many ligaments, multiple daughter droplets form from a large droplet. In some cases, satellite droplets are also seen. For some ligaments, a small narrow-sized ligament breaks off from the main ligament under the influence of the rotational motion that further breaks off into multiple small droplets. Single ligaments shedding off single droplets can also be observed. As the Re_Γ value increases, more breakup methods are seen. In the upstream region, we see that

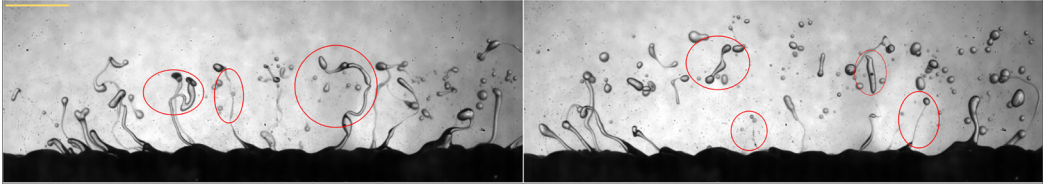


FIG. 20. Different forms of ligaments and droplet formation in the upstream region for $\phi = 0.21$ at $Re_\Gamma = 12\,150$ shown at two different instances. The scale bar represents 5 mm.

the ligaments are always under a circulatory motion that continuously stretches it inward, exerting forces on the droplet to further give up daughter droplets (Fig. 20). For $\phi = 0.21$, a greater amount of oil is taken out from the upstream region rather than the downstream penetration of the vortex ring. This is because the porosity of the uniform surface is very low, and most of the vortex ring recirculates in the upstream regime, as discussed in Sec. III D 1. Another aspect of vortical cleaning to be noted here is that the cleaning from upstream and downstream regions does not occur at the same time (check supplemental movies 9–13 [50]). Initially, the vortex ring on hitting the porous surface imparts an impulsive force that pushes the fluid at the central region downstream. The oil bag formed may rupture even before the upstream process of oil shearing starts (see, for instance, Fig. 19, $Re_\Gamma = 14\,260$ at $t^* = 14.5$). This is followed by the shearing off of the oil layer. The spreading of the vortex ring plays an important role in the upstream shearing of the oil along with the ϕ value. This spreading is responsible for taking out the oil from the holes that are present beyond the initial diameter of the incoming vortex ring. The stronger the vortex is, the more oil the vortex ring is able to take out, resulting in more ligaments and droplets.

For $\phi = 0.41$, at $Re_\Gamma = 10\,640$, a small hole (marked in Fig. 21) grows to form a large hole with the mass getting accumulated at the rim that is clearly visible at $t^* = 14.4$ in Fig. 21. Contemporarily, multiple holes occur, resulting in the total breakup of the sheet. Multiple bags are formed (~ 3) at the same time, but the rupturing time varies for each bag. Here, we consider only the bag that is formed at the center plane, and we try to estimate the rupture time for $\phi = 0.41$ using two methods: (i) Reynolds lubrication theory approximations, and (ii) time-dependent kinematics arguments. The rupture time is defined from an initial state of the oil until the first hole is observed from shadowgraphy images. In the lubrication theory model, as suggested in Platikanov [54], the thin oil film is considered to be plane-parallel from which the oil is pushed out on the application of pressure. The integration of the Reynolds equation for the rate of thinning of the film with respect to time is given as [54]

$$\int d(1/\delta_o^2) = \int \frac{4P}{3\mu r_o^2} dt. \quad (7)$$

The timescale τ obtained after the integration can therefore be expressed as

$$\tau \sim \frac{3\mu r_o^2}{4P\delta_o^2}, \quad (8)$$

where δ_o is the initial thickness of the oil layer calculated using Eq. (9), r_o is the lengthscale of the hole at the time of the first rupture, and P is the combination of capillary pressure and the disjoining pressure. Here, disjoining pressure has been neglected, and the capillary pressure has been calculated using the Young-Laplace equation. The curvature of the bag corresponding to the plane inside the page has been neglected. The initial thickness of the oil (δ_o) is found using the mass conservation principle for a layer of oil between the beads as shown below:

$$V_0 = A_b \times \delta, \quad (9)$$

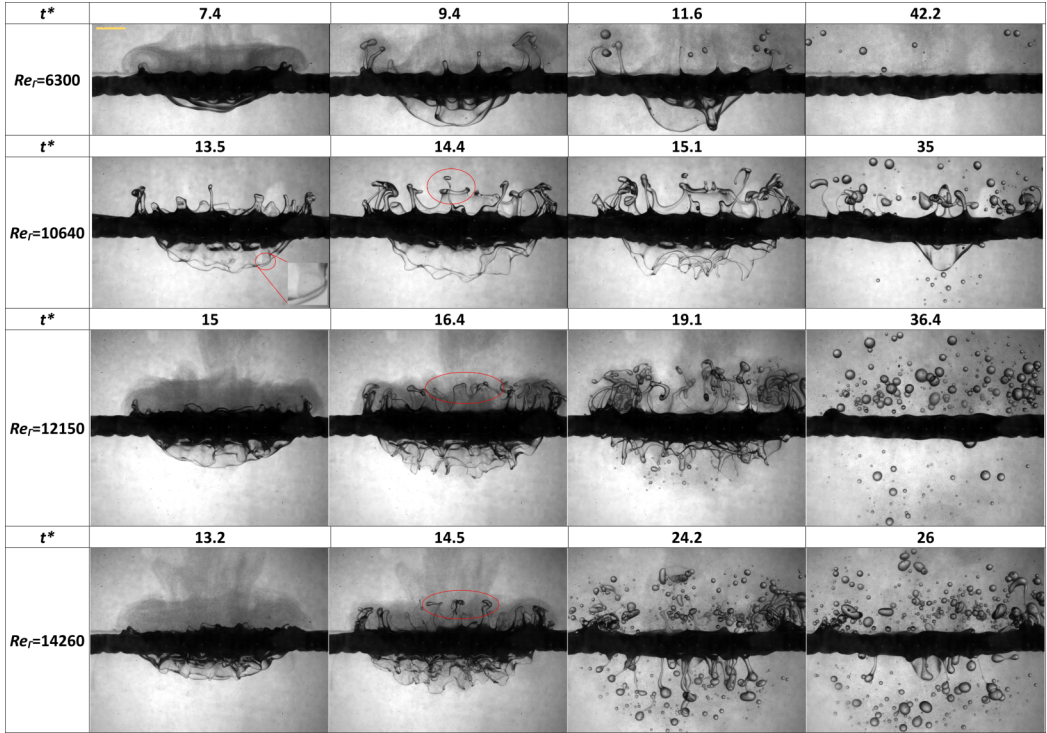


FIG. 21. Shadowgraphy images for $\phi = 0.41$ with oil at different Re_Γ shown at various t^* . The scale bar represents 5 mm. The marked zone for $Re_\Gamma = 10640$ at $t^* = 13.5$ shows the initiation of the first hole. For $Re_\Gamma = 10640$ at $t^* = 14.4$, $Re_\Gamma = 12150$ at $t^* = 16.4$ and $Re_\Gamma = 14260$ at $t^* = 14.5$, the marked area shows the accumulation of oil at the heads in the upstream region.

where V_o is the initial volume inside a hole for $\phi = 0.41$ that can be calculated using simple mensuration concepts, A_b is the surface area of the bag at any instant, and δ is the thickness of the oil layer at that instant. As discussed before, the shape of the oil bag coming out of the nonuniform porous surface before rupture resembles a semiellipsoidal shape (see Fig. 22), and its

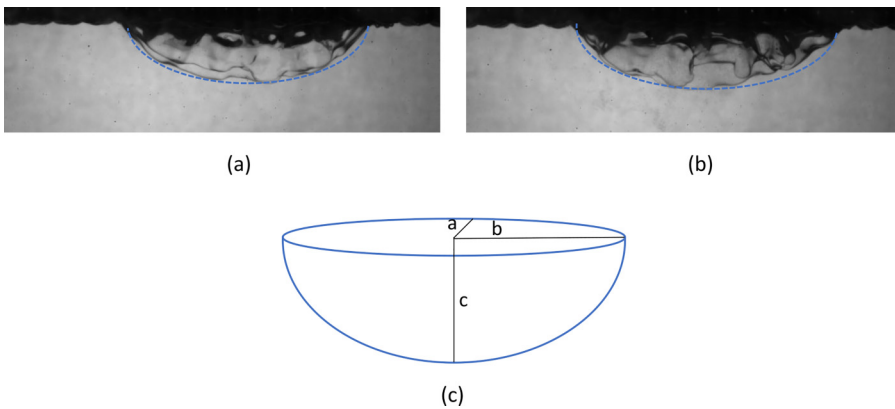


FIG. 22. Oil bag formation for (a) $Re_\Gamma = 10640$ (b) Oil bag formation for $Re_\Gamma = 12150$. The dashed blue curve is fitted in the shape of a semi-ellipsoid as shown in (c) for $\phi = 0.41$.

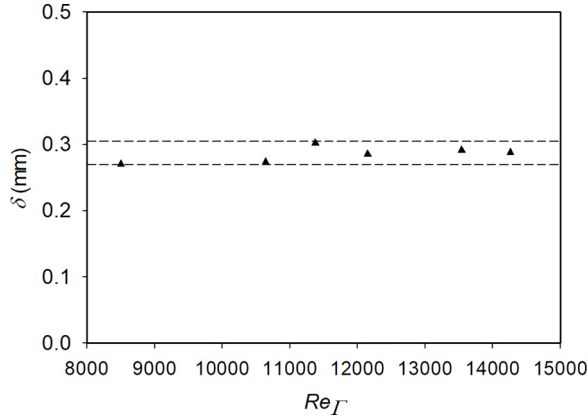


FIG. 23. Thickness of the oil bag just before rupturing for $\phi = 0.41$.

area is calculated using the Knud-Thomsen’s formula given as

$$A_b = 2\pi \left[\frac{(ab)^q + (bc)^q + (ac)^q}{3} \right]^{\frac{1}{q}}, \quad (10)$$

where a , b , and c are the dimensions of the semiellipsoid as shown in Fig. 22 and they are calculated by processing shadowgraphy images in the ImageJ software. The value of q is a constant equal to 1.6075. In the present study, the thickness of the oil bag at the time of rupture for a nonuniform bag is found to be in the range of 0.27–0.3 mm, as shown in Fig. 23.

Figure 24(a) shows a comparison between the actual and predicted rupture time of the bag for $\phi = 0.41$ at different values of Re_Γ . As expected, with an increase in the vortex strength, the time of rupture goes on decreasing. The gradient is steeper initially, and slowly tends to become constant. The predicted data are able to capture the trend well for all the Re_Γ values. At lower values of Re_Γ , i.e., in the laminar vortex regime, the model predicts the time of rupture with excellent accuracy. Here, τ represents the thin-film instability timescale that very well matches the timescale of rupture seen in the present study. The lengthscale used here is that of an initial hole formed on the bag where this analysis is meaningful. It is worth mentioning that during the time of rupture for $\phi = 0.41$, the oil layer remains highly nonuniform, and Eq. (9) remains valid everywhere on the

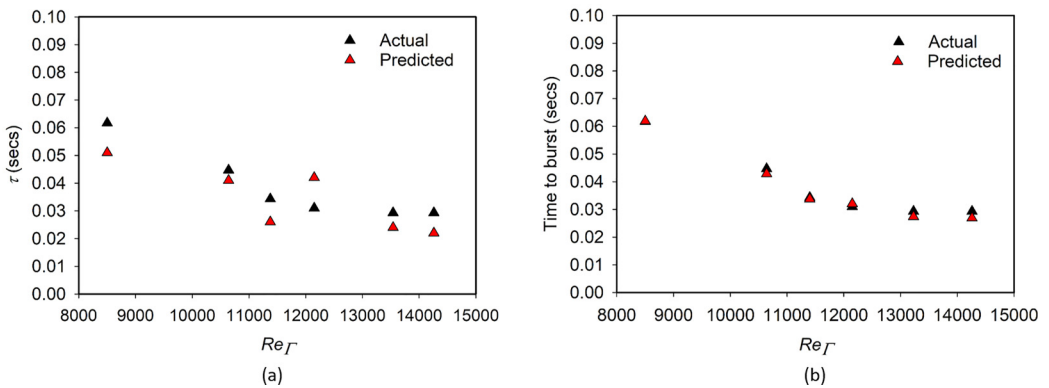


FIG. 24. Time of rupture calculated using (a) Lubrication theory estimation using Eq. (8), (b) kinematic arguments using Eq. (11).

oil layer. As we define the rupture time until the first hole occurs, Eq. (9) has been applied at that instance only.

Another method used to predict the time of rupture is by employing simple filling rate kinematics. Motivated by the experimental data, it was initially assumed that the stagnation pressure created by the incoming vortex ring varies inversely with the rupture time. On further manipulations, as shown below, we obtain a timescale for rupture using purely kinematic arguments,

$$\tau \sim \frac{\dot{m}}{P_{\text{stag}}L} \sim \frac{\rho_w AV_{\text{in}}}{1/2\rho_w V_{\text{in}}^2 L} \sim \frac{A}{V_{\text{in}}L}, \quad (11)$$

where P_{stag} is the stagnation pressure, A is the projected area of the oil initially inside the beads, V_{in} is the inlet velocity for the bag considered at the center line of the vortex ring, and L is the relevant lengthscale, i.e., the gap between the beads (4 mm). Equation (11) predicts the time of rupturing with great accuracy for all the cases, as shown in Fig. 24(b). It can be seen that no fluid property has been included in Eq. (11), making it specific for the present problem. This formula may not work in other cases having different types of fluids and porous surfaces.

The rupturing phenomenon of the oil bag for $\phi = 0.41$ is different from what was observed in $\phi = 0.21$. Most of this is because of the difference in the pore shape of the two porous surfaces considered. From Fig. 21 and supplementary movies 12-13 [50], it can be seen that after the initial hole generation, multiple sites develop a hole that results in most of the mass getting accumulated at the rim of the hole. As the hole continues to expand, the liquid rim starts to destabilize [51] leading to the formation of ligaments or fingerlike structures followed by droplets. A striking feature in the upstream oil cleansing for $\phi = 0.41$ is that initially, along with oil ligaments, uniform layers of oil sheet are formed instead of only the oil ligaments, as was seen in the case of $\phi = 0.21$. For the sheet to rise higher in the upstream region, the vortex ring must possess sufficient strength after interaction, which is seen here for $\text{Re}_\Gamma \geq 10\,640$. For ligaments, as they are stretched, they continuously thin down, resulting in a collapse to droplets when the aspect ratio becomes larger than π . In the case of upstream sheets, as they are sheared off, the oil accumulates at their heads to form a rimlike structure (Fig. 21, $\text{Re}_\Gamma = 10\,640$, $t^* = 14.4$; $\text{Re}_\Gamma = 12\,150$, $t^* = 16.4$; $\text{Re}_\Gamma = 14\,260$, $t^* = 14.5$). These rimlike structures occur due to the tension at the interface of oil and water [53]. Due to the expansion and external forcing of the sheet, this rim is perturbed, which results in azimuthal instability along its perimeter. This structure, after sufficient thinning of the sheet, starts to form cylindrical ligaments leading to the onset of the Rayleigh-Taylor instability [51–53] that consequently pinches off under the action of rotational forces collapsing into much larger droplets (Fig. 21, $\text{Re}_\Gamma = 10\,640$, $t^* = 35$; $\text{Re}_\Gamma = 12\,150$, $t^* = 36.4$; $\text{Re}_\Gamma = 14\,260$, $t^* = 26$) compared to the $\phi = 0.21$ case. The sheet continuously rotates along with the vortex ring (check supplementary movies 11–13 [50]) after the interaction that makes the rim rotate and bend towards the center line before breaking off at the neck and forming large cylindrical ligaments. The formation of sheetlike structures in the upstream region is because of the cuboid-type shape of the hole in the nonuniform porous surface that allows the vortex ring with sufficient energy to take out the oil in that shape and to evolve into a sheet. In the case of a uniform porous surface, on the contrary, oil is primarily sucked up from single holes that directly evolve to form ligaments and ultimately the droplets. As expected even for $\phi = 0.41$ the amount of oil extracted downstream increases as we increase Re_Γ . For example, at $t^* = 24.2$ for $\text{Re}_\Gamma = 14\,260$, we see a large number of ligaments that are formed after the breakup of the bag. These ligaments, as discussed previously, give out droplets of a different nature. Because of higher porosity, more oil is pushed downward in this case, hence the size of the ligaments is larger, which consequently results in the shedding of larger droplets.

IV. SUMMARY AND CONCLUSION

The interaction of vortex rings at different Re_Γ with a porous surface with and without oil was studied for $\phi = 0.21$ (uniform) and 0.41 (nonuniform). The aim was to develop an idea of vortical

cleaning where the kinetic energy of the vortex ring is harnessed to expunge oil out of the porous surface.

For cases with no oil, the flow features both upstream and downstream of the porous surface were found to be different for $\phi = 0.21$ and 0.41 . The effect of ϕ on the incoming vortex ring was found to be much less and has been ignored in the present study. The upstream core dissipates slowly for $\phi = 0.21$ compared to $\phi = 0.41$ because of the less open surface area at lower Re_Γ values, and it shows a complex dependency on the shape and ϕ is observed. We see a reversal in the rate of kinetic energy dissipation after a certain nondimensional time (t_k^*) that is attributed to the dominating factor (ϕ and Re_Γ) at that t_k^* value. The flow in the downstream comes out as small individual jets for $\phi = 0.21$, whereas a continuous sheet of water emerges for $\phi = 0.41$. This is because of the shape of the hole in the nonuniform-type porous surface. KH instability is responsible for chaotic flow mixing resulting in highly three-dimensional flow behavior. The vorticity cancellation mechanism plays an important role in the formation of the regenerated vortex ring.

For oil-laden porous surfaces, the interaction process was divided into three steps: (i) the penetration regime, (ii) bag formation, and (iii) bag breakup. The effect of placing a porous surface soaked in oil on the uninteracted vortex ring showed similar trends to those seen by placing a solid wall. For $\phi = 0.21$ the vortex ring is able to rupture the cylindrical-shaped oil bag for $Re_\Gamma \geq 10\,640$. The heads of the oil bag develop a hole due to the continuous thinning of the oil layer resulting in its rupture. At higher Re_Γ , rim destabilization leads to the formation of ligaments due to the Rayleigh-Taylor instability that further sheds droplets due to Rayleigh-Plateau-type instability. The oil is taken out from the upstream side as well, where ligaments of various shapes and features develop pinching off droplets in different manners. The external environment being turbulent and rotational makes the ligaments rotate about the center line, making the droplet pinch-off process complicated. More oil is taken out from the upstream region rather than the downstream region for $\phi = 0.21$.

For $\phi = 0.41$, a large bag of oil is formed downstream due to the large open area that further develops holes at different sites (for $Re_\Gamma \geq 10\,640$) before the formation of ligaments and droplets. The trend of the movement of the oil layer downstream in the penetration regime was predicted using appropriate scaling of the NS equation. The rupture time was estimated using the lubrication theory estimations and a kinematic formulation consistent with the present study. The thickness at which the rupture occurs was calculated to be in the range of 0.27 – 0.3 mm using the principles of conservation of mass. In the upstream region (for $\phi = 0.41$), along with ligaments, neat sheets of oil layer are formed. Accumulation of oil mass at the rim of this sheet due to interfacial tension and its further expansion lead to the formation of ligaments (Rayleigh-Taylor instability) and larger-sized droplets (Rayleigh-Plateau-type instability) compared to $\phi = 0.21$.

The present study was conducted to test if the vortex ring was able to take out the oil from two different types of porous surfaces. Such a study has never been reported before, and to develop a concrete understanding of the process, more studies need to be conducted. However, the study has been revealing enough to conclude that vortex rings, especially those having higher strength, can be exploited to clean porous surfaces. The shape and porosity of the porous surface play a crucial role in deciding the path in which the final droplets are formed. The cleaning takes place from both the upstream and downstream sides of the porous surface, which is due to the rotational nature of the vortex ring and may not be obtained if water jets are used instead of vortex rings. A similar concept can be applied for cleaning surgical masks in an air medium and other porous surfaces countered in industrial and household settings. In our future studies, we aim to develop a more rigorous mathematical framework to understand the bag formation and rupturing process along with quantifying the cleaning process by finding the cleaning efficiency.

ACKNOWLEDGMENTS

S.B. acknowledges funding received through DRDO Chair Professorship. S.J. acknowledges funding received through the Prime Minister's Research Fellowship scheme.

- [1] T. T. Lim and T. B. Nickels, *Fluid Vortices*, edited by S. I. Green (Springer Netherlands, Dordrecht, 1995), pp. 95–153.
- [2] J. O. Dabiri, S. P. Colin, J. H. Costello, and M. Gharib, Flow patterns generated by oblate medusan jellyfish: field measurements and laboratory analyses, *J. Exp. Biol.* **208**, 1257 (2005).
- [3] T. S. Lundgren, J. Yao, and N. N. Mansour, Microburst modelling and scaling, *J. Fluid Mech.* **239**, 461 (1992).
- [4] A. Per M., J. K. Sandor, T. Johannes, B. Rasmus, E. Heiberg, M. Carlsson, and H. Arheden, Vortex ring behavior provides the epigenetic blueprint for the human heart, *Sci. Rep.* **6**, 22021 (2016).
- [5] P. G. Saffman, The velocity of viscous vortex rings, *Stud. Appl. Math.* **49**, 371 (1970).
- [6] T. Maxworthy, The structure and stability of vortex rings, *J. Fluid Mech.* **51**, 15 (1972).
- [7] S. E. Widnall, J. P. Sullivan, and P. R. Owen, On the stability of vortex rings, *Proc. R. Soc. London, Ser. A* **332**, 335 (1973).
- [8] N. Didden, On the formation of vortex rings: Rolling-up and production of circulation, *Z. Angewandte Math. Phys. ZAMP* **30**, 101 (1979).
- [9] A. Glezer, The formation of vortex rings, *Phys. Fluids* **31**, 3532 (1988).
- [10] M. Gharib, E. Rambod, and K. Shariff, A universal time scale for vortex ring formation, *J. Fluid Mech.* **360**, 121 (1998).
- [11] M. Shusser and M. Gharib, Energy and velocity of a forming vortex ring, *Phys. Fluids* **12**, 618 (2000).
- [12] I. S. Sullivan, J. J. Niemela, R. E. Hershberger, D. Bolster, and R. J. Donnelly, Dynamics of thin vortex rings, *J. Fluid Mech.* **609**, 319 (2008).
- [13] A. Tinaikar, S. Advait, and S. Basu, Understanding evolution of vortex rings in viscous fluids, *J. Fluid Mech.* **836**, 873 (2018).
- [14] D. Adhikari and T. T. Lim, The impact of a vortex ring on a porous screen, *Fluid Dyn. Res.* **41**, 051404 (2009).
- [15] J. T. Hrynuik, J. Van Luipen, and D. Bohl, Flow visualization of a vortex ring interaction with porous surfaces, *Phys. Fluids* **24**, 037103 (2012).
- [16] C. Naaktgeboren, P. S. Krueger, and J. L. Lage, Interaction of a laminar vortex ring with a thin permeable screen, *J. Fluid Mech.* **707**, 260 (2012).
- [17] M. Cheng, J. Lou, and T. T. Lim, A numerical study of a vortex ring impacting a permeable wall, *Phys. Fluids* **26**, 103602 (2014).
- [18] M. N. Musta and P. S. Krueger, Interaction of vortex rings with multiple permeable screens, *Phys. Fluids* **26**, 113101 (2014).
- [19] A. Mujal-Colilles, S. B. Dalziel, and A. Bateman, Vortex rings impinging on permeable boundaries, *Phys. Fluids* **27**, 015106 (2015).
- [20] J. T. Hrynuik, C. M. Stutz, and D. G. Bohl, Experimental measurement of vortex ring screen interaction using flow visualization and molecular tagging velocimetry, *J. Fluids Eng.* **140**, 111401 (2018).
- [21] X. An, L. Jiang, and F. Hassanipour, Numerical analysis of air vortex interaction with porous screen, *Fluids* **6**, 70 (2021).
- [22] Y. Xu, Z.-Y. Li, J.-J. Wang, and L.-J. Yang, On the interaction between turbulent vortex rings of a synthetic jet and porous walls, *Phys. Fluids* **31**, 105112 (2019).
- [23] Y. Xu, J.-J. Wang, L.-H. Feng, G.-S. He, and Z.-Y. Wang, Laminar vortex rings impinging onto porous walls with a constant porosity, *J. Fluid Mech.* **837**, 729 (2018).
- [24] Z.-Y. Li, Y. Xu, L.-H. Feng, and J.-J. Wang, Synthetic jet vortex rings impinging onto a porous wall: Reynolds number effect, *Int. J. Heat Mass Transf.* **137**, 951 (2019).
- [25] Z.-Y. Li, Y. Xu, and J.-J. Wang, Similarity parameter for synthetic jet vortex rings impinging onto porous walls, *AIAA J.* **58**, 722 (2020).
- [26] Y. Xu, Z.-Y. Li, and J.-J. Wang, Experimental investigation on the impingement of synthetic jet vortex rings onto a porous wall, *Phys. Fluids* **33**, 035140 (2021).
- [27] E. Villermaux, Fragmentation, *Annu. Rev. Fluid Mech.* **39**, 419 (2007).
- [28] E. Villermaux and B. Bossa, Drop fragmentation on impact, *J. Fluid Mech.* **668**, 412 (2011).
- [29] S. Sharma, A. P. Singh, and S. Basu, On the dynamics of vortex–droplet co-axial interaction: insights into droplet and vortex dynamics, *J. Fluid Mech.* **918**, A37 (2021).

- [30] S. Sharma, R. Pinto, A. Saha, S. Chaudhuri, and S. Basu, On secondary atomization and blockage of surrogate cough droplets in single- and multilayer face masks, *Sci. Adv.* **7**, eabf0452 (2021).
- [31] S. Sharma, A. Pratap Singh, S. Srinivas Rao, A. Kumar, and S. Basu, Shock induced aerobreakup of a droplet, *J. Fluid Mech.* **929**, A27 (2021).
- [32] G. I. Taylor, The dynamics of thin sheets of fluid. iii. disintegration of fluid sheets, *Proc. R. Soc. London A* **253**, 313 (1959).
- [33] F. E. C. Culick, Comments on a ruptured soap film, *J. Appl. Phys.* **31**, 1128 (1960).
- [34] W. E. Ranz, Some experiments on the dynamics of liquid films, *J. Appl. Phys.* **30**, 1950 (1959).
- [35] C. Vernay, L. Ramos, and C. Ligoure, Free radially expanding liquid sheet in air: Time- and space-resolved measurement of the thickness field, *J. Fluid Mech.* **764**, 428 (2015).
- [36] Y. Wang and L. Bourouiba, Drop impact on small surfaces: Thickness and velocity profiles of the expanding sheet in the air, *J. Fluid Mech.* **814**, 510 (2017).
- [37] Y. Wang, R. Dandekar, N. Bustos, S. Poulain, and L. Bourouiba, Universal Rim Thickness in Unsteady Sheet Fragmentation, *Phys. Rev. Lett.* **120**, 204503 (2018).
- [38] M. Jalaal and K. Mehravaran, Fragmentation of falling liquid droplets in bag breakup mode, *Int. J. Multiphase Flow* **47**, 115 (2012).
- [39] V. Kulkarni and P. E. Sojka, Bag breakup of low viscosity drops in the presence of a continuous air jet, *Phys. Fluids* **26**, 072103 (2014).
- [40] M. Jain, R. S. Prakash, G. Tomar, and R. V. Ravikrishna, Secondary breakup of a drop at moderate weber numbers, *Proc. R. Soc. A* **471**, 20140930 (2015).
- [41] R. D. Keane and R. J. Adrian, Optimization of particle image velocimeters: II. Multiple pulsed systems, *Meas. Sci. Technol.* **2**, 963 (1991).
- [42] K. Rajamanickam and S. Basu, On the dynamics of vortex–droplet interactions, dispersion and breakup in a coaxial swirling flow, *J. Fluid Mech.* **827**, 572 (2017).
- [43] K. Shariff and A. Leonard, Vortex rings, *Annu. Rev. Fluid Mech.* **24**, 235 (1992).
- [44] N. K. Jha and R. Govardhan, Interaction of a vortex ring with a single bubble: Bubble and vorticity dynamics, *J. Fluid Mech.* **773**, 460 (2015).
- [45] M. Dziedzic and H. J. Leutheusser, An experimental study of viscous vortex rings, *Exp. Fluids* **21**, 315 (1996).
- [46] A. Weigand and M. Gharib, Turbulent vortex ring/free surface interaction, *J. Fluids Eng.* **117**, 374 (1995).
- [47] J. D. A. Walker, C. R. Smith, A. W. Cerra, and T. L. Doligalski, The impact of a vortex ring on a wall, *J. Fluid Mech.* **181**, 99 (1987).
- [48] P. Orlandi, Vortex dipole rebound from a wall, *Phys. Fluids* **2**, 1429 (1990).
- [49] C. Chu, C. Wang, and C. Hsieh, An experimental investigation of vortex motions near surfaces, *Phys. Fluids* **5**, 662 (1993).
- [50] See Supplemental Material at <http://link.aps.org/supplemental/10.1103/PhysRevFluids.8.044701> for supplementary movies 1–13 and supplementary figures S1 and S2.
- [51] B. E. Scharfman, A. H. Techet, J. W. M. Bush, and L. Bourouiba, Visualization of sneeze ejecta: steps of fluid fragmentation leading to respiratory droplets, *Exp. Fluids* **57**, 24 (2016).
- [52] A. L. Yarin, I. V. Roisman, and C. Tropea, *Collision Phenomena in Liquids and Solids* (Cambridge University Press, Cambridge, 2017).
- [53] D. Roy, S. M. A. Rasheed, P. Kabi, A. S. Roy, R. Shetty, and S. Basu, Fluid dynamics of droplet generation from corneal tear film during non-contact tonometry in the context of pathogen transmission, *Phys. Fluids* **33**, 092109 (2021).
- [54] D. Platikanov, Experimental investigation on the “dimpling” of thin liquid films, *J. Phys. Chem.* **68**, 3619 (1964).